DYNAMIC PHASOR MODELING OF TYPE 3 WIND TURBINE GENERATORS FOR LARGE-SCALE POWER SYSTEM TRANSIENT STABILITY STUDIES

by

Wonbae Choi

B.S., Hanyang University, 2010

A THESIS SUBMITTED IN PARTIAL FULFILLMENT OF

THE REQUIREMENTS FOR THE DEGREE OF

MASTER OF APPLIED SCIENCE

in

THE FACULTY OF GRADUATE AND POSTDOCTORAL STUDIES

(Electrical and Computer Engineering)

THE UNIVERSITY OF BRITISH COLUMBIA

(Vancouver)

September 2017

Abstract

The wind power penetration has been increasing significantly, and this trend is likely to continue. As wind power penetration levels increase, interconnecting large-scale wind power plants (WPPs) into the existing power system has become a critical issue. Therefore, appropriate wind turbine generator models are required to conduct transient stability (TS) studies. While it is possible to construct detailed and accurate models of manufacturer-specific wind turbine generators in electromagnetic transient (EMT) simulators, such models are not suitable for large-scale transient stability studies due to their high computational complexity. The Western Electricity Coordinating Council (WECC) Renewable Energy Modeling Task Force (REMTF) is working towards developing generic wind turbine generator models that would be applicable for a range of general purpose system-level studies. However, such the generic models are typically over-simplified and not able to predict some of the phenomena, e.g. the unbalanced disturbance which is easily captured by the EMT simulations.

In this research, a numerically-efficient model for the doubly-fed induction generator (DFIG) is developed that can predict steady state, balanced and unbalanced disturbances, and is sufficiently generic. The new DFIG model is based on the dynamic-phasor (DP) based machine models, which have been recently developed for the EMT simulators and can work with fairly large time-steps (up to several milliseconds) approaching that of the TS program solution.

The WPP models have been implemented in MATLAB/Simulink® to assess the improved accuracy and computational efficiency. The new DP-based DFIG model is tested in a single

machine infinite bus case and a two-area four-machine network to validate the model's responses to balanced and unbalanced conditions of the grid. The accuracy of new DFIG model is shown to be significantly better compared to traditional TS models, which is achieved at a slightly increased computational cost.

The result of this research will provide more accurate dynamic phasor based models of WPP for TS analysis. Since TS programs are widely used by utilities over the world, the new DP-based DFIG model will contribute to more reliable and accurate studies. This, in turn, will enable more reliable integration of large-scale WPPs into the existing and expanding power grids.

Lay Summary

As the penetration of wind power increases, interconnecting wind power plants (WPPs) into the existing power system becomes a critical issue. Therefore, accurate and computationally efficient models of wind turbine generators are required.

In my research, a numerically-efficient model of doubly-fed induction generator (DFIG) is developed based on dynamic phasor formulation. The accuracy of new DFIG model is shown to be significantly better compared to traditional transient stability (TS) models, which is achieved at a slightly increased computational cost.

The result of this research will provide more accurate dynamic phasor based models of WPP for TS analysis. Since TS programs are widely used by utilities over the world, the new DP-based DFIG model will contribute to more reliable and accurate studies. This, in turn, will enable wider and more reliable integration of large-scale WPPs into the existing and expanding power grids.

Preface

This thesis is original and independent work by the author, Mr. Wonbae Choi. All models and simulation results included in this thesis have been produced by the author. This research work has been done by Mr. Wonbae Choi under the supervision of Dr. Juri Jatskevich. Some of the material included in the thesis may be submitted for publication:

W. Choi, Y. Huang, and J. Jatskevich, "Dynamic Phasor Modelling of Type-3 Wind Turbine Generator for Transient Stabilities Considering Unbalanced Operation," In Preparation for *IEEE Power and Energy Society General Meeting (PES GM 2018)*, August 2018, Portland OR, USA.

Table of Contents

List of Tables

List of Figures

List of Symbols

i_{as}, i_{bs}, i_{cs}	Phase-a, b and c stator current of induction machines
i_{ds}, i_{qs}	*d*, *q*-axis stator current of induction machines
i_{ar}, i_{br}, i_{cr}	Phase-a, b and c rotor current of induction machines
i_{dr}, i_{qr}	*d*, *q*-axis rotor current of induction machines
v_{as}, v_{bs}, v_{cs}	Phase-a, b and c stator voltage of induction machines
v_{ds}, v_{qs}	*d*, *q*-axis stator voltage of induction machines
v_{ar}, v_{br}, v_{cr}	Phase-a, b and c rotor voltage of induction machines
v_{dr}, v_{qr}	*d*, *q*-axis rotor voltage of induction machines
$\psi_{as}, \psi_{bs}, \psi_{cs}$	Phase-a, b and c stator flux of induction machines
ψ_{ds}, ψ_{qs}	*d*, *q*-axis stator flux of induction machines
$\psi_{ar}, \psi_{br}, \psi_{cr}$	Phase-a, b and c rotor flux of induction machines
ψ_{dr}, ψ_{qr}	*d*, *q*-axis rotor flux of induction machines
C_p	Power coefficient of wind turbine blade
f_s	Stator frequency of induction machines, fundamental frequency of a network
f_r	Rotor frequency of induction machines
p	Number of poles (even number lager than 2)
ω_s	Synchronous speed of the *dq* reference frame, stator angular frequency
ω_r	Rotor electrical angular speed
ω_m	Rotor mechanical angular speed
ω_t	turbine shaft speed

ω_{sl}	Angular slip frequency
P_s, P_r	Stator and rotor power of DFIG
P_t	Total power output of DFIG
R_s	Stator resistance of induction generator
L_s	Stator self-inductance of induction generator
L_{ls}	Stator leakage inductance of induction generator
R_r	Rotor resistance of induction generator
L_r	Rotor self-inductance of induction generator
L_{lr}	Rotor leakage inductance of induction generator
L_m	Magnetizing inductance of induction generator

Glossary

DFIG	Doubly Fed Induction Generator
DP	Dynamic Phasor
EMT	Electromagnetic Transient
FRT	Fault Ride Through
GSC	Grid Side Converter
IGBT	Insulated Gate Bipolar Transistor
MMF	Magneto Motive Force
NREL	National Renewable Energy Laboratory
POI	Point of Interconnection
ROM	Reduced-order Model
RSC	Rotor Side Converter
SMIB	Single Machine Infinite Bus
VBR	Voltage Behind transient Reactance
VSC	Voltage Source Converter
WECC	Western Electricity Coordinating Council
WECS	Wind Energy Conversion System
WPP	Wind Power Plant

Acknowledgements

My deep gratitude goes first to my supervisor Dr. Juri Jatskevich, who expertly guided me through my graduate education and who shared his extensive knowledge about power systems modeling and simulation. His unwavering enthusiasm for power systems kept me constantly engaged with my research and his personal generosity helped make my time at UBC enjoyable. I also would like to thank the examining committee members, Dr. Herman Dommel and Dr. Jose Marti for their time, valuable discussions and advice, which have contributed to the quality of my work.

My appreciation also extends to my fellow graduate students and colleagues from the Electric Power and Energy Systems research group at UBC, who have shared their experience and have inspired me to continue my work in this field. They made my student life a lot better.

Special thanks are owed to my parents and in-laws, whose have supported me throughout my years of education, especially for my mother who devoted her life to always giving her children the best. I would like to also thank to my sister and her family members and sister-in-law to encourage me all the time.

Most of all, this great journey wouldn't have been possible without my beloved wife, Kyung Eun Han, and my son Juno. You are my true inspiration and motivation to go extra miles.

Dedicated to my beloved wife, Kyung Eun Han,

adorable son, Juno,

and soon-to-be-born new family member

Chapter 1: Introduction

1.1 Background and Motivation

Renewable energy is expected to provide 80% of the total electricity in the US by 2050, and half of that will come from wind and solar power [1]. In this trend, it is very important to analyze the impact of increasing wind power plants (WPP) on the existing power grid. The dynamic behavior of WPP is very different from that of conventional power plants; therefore, it requires special consideration, detailed interconnection studies, and efficient modeling approaches. Various modeling and simulation techniques have been used to conduct relevant studies including feasibility studies and system impact studies for interconnecting the WPP into the grid. The accuracy of system studies depends on the fidelity of the underlying models. Studies and models that give overly-optimistic results may miss some important phenomena and lead to wide-spread power outages, whereas studies that give overly-conservative results may lead to inefficient grid operation and unutilized resources [2].

Since the electric grid consists of power generation, transmission and power distribution, and loads, all of which makes up a very large and complicated network with very wide range of dynamics, its modeling and analysis is also difficult and complex. Depending on the time frame of interests, different modelling techniques should be applied. "All models are wrong, but some are useful" is the famous quotes in statistics which emphasizes the importance of the modeling techniques [3].

Therefore, developing computationally efficient and sufficiently accurate models of wind generators for large scale bulk power systems has been a primary research and is a goal of this thesis.

1.2 Types of Commonly used Wind Energy Conversion Systems

Although wind energy has been used by the mankind for hundreds of years for various purposes, it has been only 30 years that the wind energy has become a reliable means to produce electricity efficiently thanks to the advanced technologies [4]. The major components of a typical wind energy conversion system include the follows:

- Wind turbine
- Generator
- Control & Protection systems
- Interconnection equipment
- Power Electronic Converters (if applicable)

Depending on how and what kind of components are used, the Western Electricity Coordinating Council (WECC) classifies the wind turbine generators into four different types [5].

As shown in Figure 1.1, Type 1 wind turbine generator is simply a squirrel-cage induction generator (SCIG) directly connected to the grid via a step up transformer. In this case, the turbine speed is nearly fixed to the electrical grid frequency. It generates real power when the turbine speed is faster than the electrical grid frequency creating a negative slip. For sudden changes in wind speed, the rate of change in electrical output is limited by mechanical inertia of the drive train.

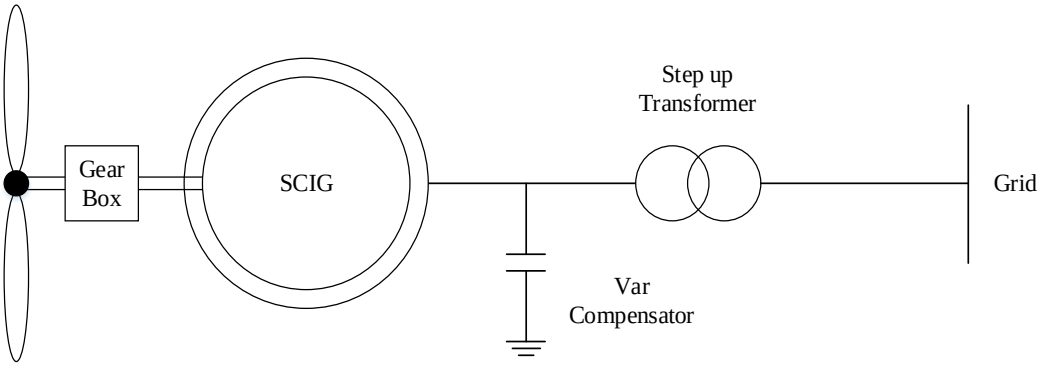

Figure 1.1 Type 1 Wind Turbine Generator Configuration.

The Type 2 wind turbine generator consists of a wound rotor induction generator (WRIG) with a variable resistor in the rotor circuit, but its stator is directly connected to the grid via a step up transformer as shown in Figure 1.2. Since the variable resistors are connected to the rotor circuit, the Type 2 wind turbine generator can control the rotor currents quickly by adjusting the rotor resistance so that the output power can be stable for small wind speed variation. This configuration will affect the dynamic response during grid disturbance.

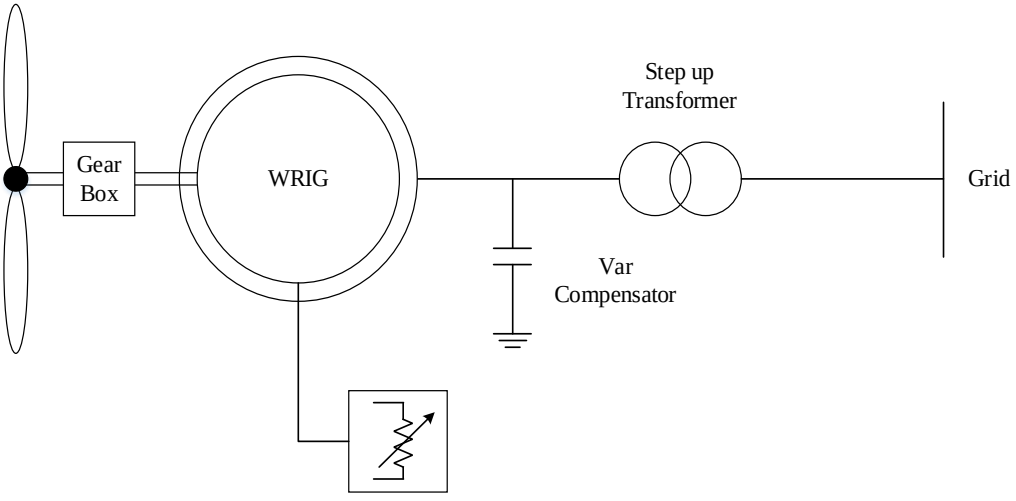

Figure 1.2 Type 2 Wind Turbine Generator Configuration.

The Type 3 wind turbine generator has become most popular configuration for the last several decades, which is also known as a double-fed induction generator (DFIG). Compared to the Type 2 wind turbine generator, the rotor side converter (RSC) is connected the DC link, which is then connected to the grid side converter (GSC), which makes it possible to exchange the rotor power with the grid. Since only approximately 30% of the total active power supplied by the generator goes through the rotor side, the rating of the RSC and GSC which together work the back-to-back voltage source converter (VSC), is also about 30% of the total rated power. This feature makes the Type 3 wind turbine generator very cost effective and controllable. Both Type 2 and Type 3 generator typically require a gearbox to scale the propeller speed to the generator shaft speed.

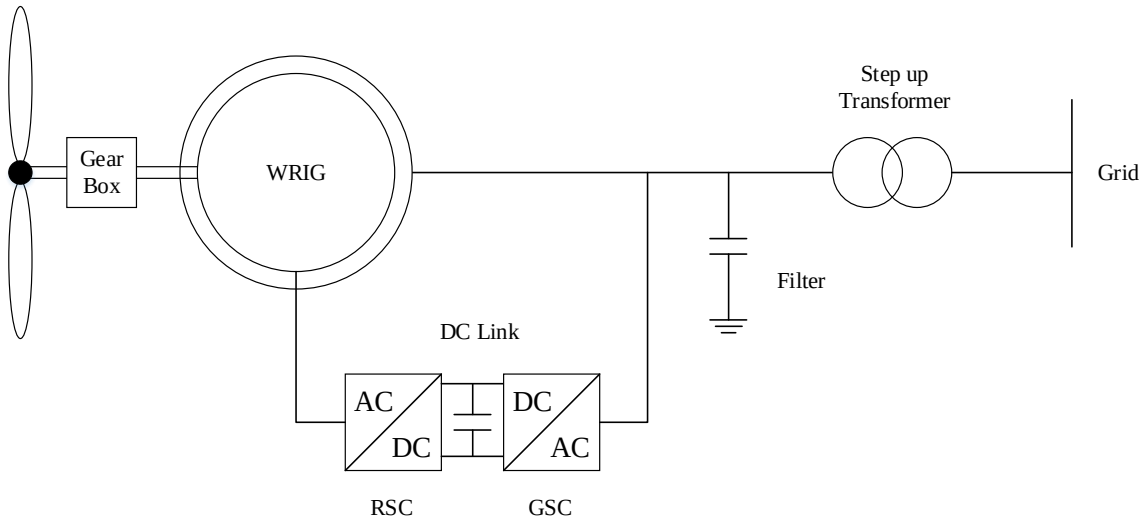

Figure 1.3 Type 3 Wind Turbine Generator Configuration.

The Type 4 wind turbine generator is connected to the grid via the back-to-back VSC as shown in Figure 1.4. Due to its unique configuration, the grid side disturbances do not affect the stator circuit of the generator directly. Also, depending on the number of magnetic poles of the synchronous or induction generator used, the gearbox can be removed as the full scale back-to-back VSC can control the electrical frequency in a wide range. However, the VSCs should be rated as high as the generator output. So, the cost of Type 4 generators is typically higher than that of the Type 3 wind turbine generators.

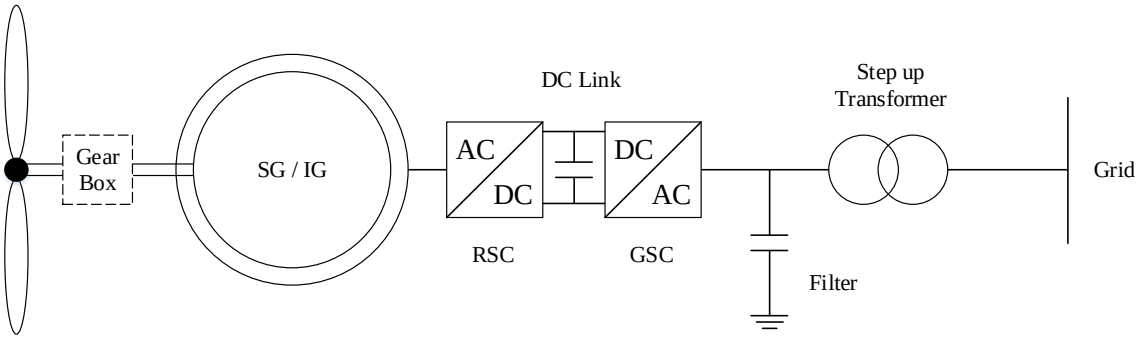

Figure 1.4 Type 4 Wind Turbine Generator Configuration.

1.3 Literature Review and State-of-the-Art

1.3.1 DFIG Modeling

Depending on the time frame of interest, modeling techniques and assumptions vary significantly. In this section, the detail and simplified modeling of the DFIG are reviewed.

1.3.1.1 EMT Time Domain Coupled Circuit Models

The most commonly used time-domain coupled-circuit model with cascaded control scheme is presented in [6]. In this article, the stator-flux-oriented vector control method is used and the detail switching dynamics of power electronic devices and dynamics of phase locked loop (PLL) are neglected, which is an acceptable assumption for the purpose of this thesis as the time frame of interest is not the fast dynamics and harmonics of power electronic devices. In [7], dynamic behavior of DFIG during grid faults is analyzed thoroughly by providing various simulation results along with relevant grid codes and detail control schemes. There are numerous literatures related to the DFIG; however, above references provide the fundamental concepts for modeling of the induction generator and converters. In [8], state-space form of 5^{th} order induction generator model and converters are presented and the model is tested in the simple network to analyze inter-area oscillation which is similar approach to this thesis.

1.3.1.2 Simplified Positive Sequence Transient Stability Models

The purpose of developing simplified phasor-domain model is to represent the electromechanical transients in the large-scale power system network since the time frame of interest is only a few seconds or longer and it would be inefficient to use full-order time-domain model to analyze this type of problem. There are many literature sources introducing simplified DFIG modeling for

positive sequence phasor-domain [9]. In [10], by neglecting the DC link voltage dynamics and stator field dynamics which are fast compared to the rotor filed dynamics, a numerically efficient DFIG model is introduced and tested in a six-machines 23-bus system. Instead of using machine circuit parameters such as R_s, R_r, X_{ls} and X_{lr}, the operational parameters such as time constants and sub-transient reactances are directly used for the reduced-order models in large-scale transient stability studies. In [11], simplification procedures for deriving the DFIG model is well explained and the final reduced-order model is demonstrated in studies with single machine infinite bus (SMIB) system. In [12], a popular GE wind turbine generator is modeled as controlled current source which neglects the stator and rotor dynamics.

The WECC Renewable Energy Modeling Task Force has developed generic models of wind turbine generators by simplifying the detailed transient stability models [13]. The developed generic reduced-order models were validated against the field measurement data [5][14][15]. Other literatures have also supported the sufficiently of the simplified phasor modeling approach [16][17][18][19].

1.3.2 Dynamic Phasor Modeling Approach for DFIG

In 1991, the dynamic phasor (DP) concept was introduced for modeling series resonant converters [20]. Since then, numerous research works have been conducted and proved the efficiency of DP approach for power electronic devices, electric machinery, and power system analysis in general.

In [21], detail research on induction machines and synchronous machines based on dynamic phasor and space-vector concept was conducted. There are other publications providing detailed dynamic modeling techniques for those machines [22][23]. Power system dynamics also can be modeled by dynamic phasors [24][25][26][27]. Moreover, the detail power electronic dynamics such as active front-end rectifier for aircraft applications [28], PV solar inverters [29], HVDC converters [30] and so on, can be well analyzed with the dynamic phasor modeling techniques.

Reference [31] is the first research on dynamic phasor modeling of DFIG which is based on machine and converter models in synchronous reference frame. The model is tested in SMIB system and simulation results were compared with the one in time domain. Reference [32] uses the same model defined in [31] but includes the sub-synchronous control interactions between series compensated network and the rotor side converter of DFIG. Previous works [31][32] are suitable for EMTP [33] level studies which can capture the electromagnetic transient. However, the objective of this thesis is to utilize the concept of dynamic phasors to develop a simplified model of DFIG that would be suitable for transient analysis of large-scale power systems.

1.4 Objective of the Thesis

The main objective of the thesis is to develop a dynamic phasor model of DFIG that is numerically efficient and yet maintains certain level of accuracy similar to the EMT models, and therefore suitable for more accurate transient stability studies of large scale power systems.

As the wind power penetration has been significantly increasing, the grid operators set up more demanding grid code requirements for wind power integration [34]. The major requirement is the wind turbine generators must be capable to stay on-line during a severe voltage dips, which is commonly referred to as the fault ride-through (FRT) capability [35]. Therefore, a traditional way to represent wind farms as negative loads are no longer valid and a new approach is required to properly represent the dynamic characteristics of wind turbine generators in system studies. The most recent and rigorous work related to the generic wind turbine modeling for transient stability studies has been done by the WECC [13]. However, the developed models have following limitations:

- The model is based on positive-sequence only, which limits its application for accurate assessment of unbalanced grid conditions.
- Potential torsional interactions between the wind turbine generator and the network cannot be evaluated.

The above-stated limitations can be resolved by applying the dynamic phasor techniques since DP approach can handle both balanced and unbalanced conditions effectively by selecting relevant frequency components. Therefore, this thesis sets forth the following objectives:

1. To derive a new dynamic-phasor-based model of DFIG and validate it by comparisons with a reference time-domain EMT model under a single machine infinite bus system.

2. To derive a DP-based reduced-order model for transient stability analysis by neglecting the stator dynamics.
3. To test the proposed reduced-order DP-based model in a simple power network [36] under balanced and unbalanced conditions.

1.5 Organization of the Thesis

Chapter 1 includes the introduction, motivation, and objectives of the thesis. Brief background information about wind energy conversion systems is provided along with their configurations. The relevant literature is reviewed and detail tasks and methodology are also narrated. In Chapter 2, the fundamentals of power system dynamics and modeling techniques are explained with examples. Through the simple examples, the advantage of dynamic phasor approach is verified. In Chapter 3, the detail mathematical modeling of DFIG with back-to-back voltage source converters are derived in both time-domain and dynamic-phasor representation including reference frame theory, maximum power point tracking (MPPT) control, wind turbine, wound rotor induction generator model. In Chapters 4 & 5, the models are simulated and verified in SMIB system and a 2-area 4-machines network. The efficiency of each model is verified by measuring a time step during balanced and unbalanced disturbances. Chapter 6 provides the summary of research, significance and contribution of the thesis along with the final conclusions. Also, some possible applications and future work are described.

Chapter 2: Power System Dynamics and Modeling

Power system modelling has been recognized as an important part in order to analyze large scale complex power system networks and problems closely related to power system stability. As power systems have evolved through interconnection with renewable energy sources, the stability analysis has become a challenging task to guarantee the safe operation of interconnected grids. Various forms of instability such as voltage stability, frequency stability and rotor angle stability are well defined and explained in [37].

2.1 Time-scales of Power System Dynamics

Depending on the speed of power system transients, the power system dynamics can be categorized into four groups: wave phenomena, electromagnetic transients (EMT), electromechanical transient, and thermodynamic phenomena, as shown in Figure 2.1 [38]. The corresponding time frame of each transient type is closely related to the modeling of power system elements in such time frame because a variety of dynamics exists in the same power network, but some of the dynamics will only affect certain parts of the system or components.

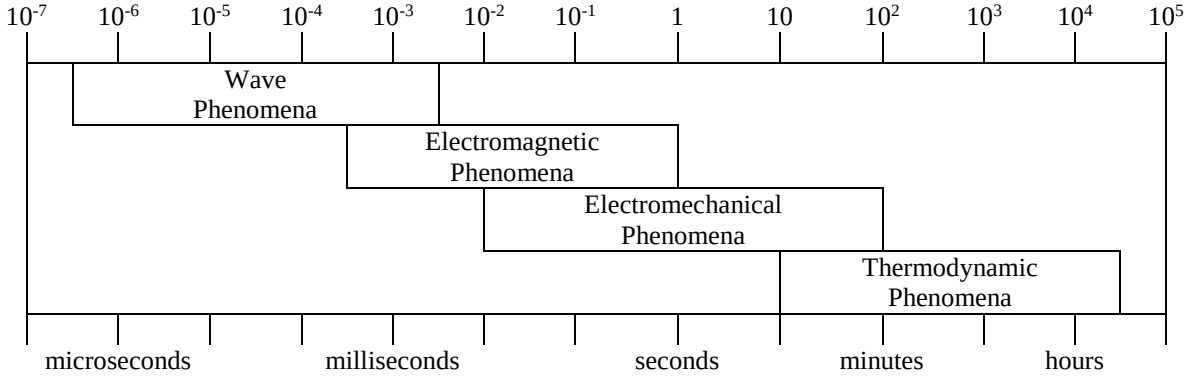

Figure 2.1 Time frame of power system dynamic phenomena [38]**.**

For example, the time frame of EMT is from milliseconds to a second, which is slower than the wave phenomena but faster than the electromechanical transients. The electromechanical transients are commonly associated with mechanical systems dynamics in power system networks and the oscillations of rotating masses of generators and motors and prime mover controls. The time frame of electromechanical transients is from a second to several seconds.

Due to increased penetration of electronically-interfaced renewable energy resources such as wind and solar, the interactions that used to be electromechanical transients and analyzed using TS tools in traditional power systems are becoming much faster and span the entire range of electromagnetic (EMT) and electromechanical phenomena. This challenge in turn necessitates creation of new models and simulation tools that have wider range of application while possessing good numerical efficiency and accuracy.

2.2 Modeling Approaches

Power systems can be categorized into generation, transmission and distribution systems, and loads. Each component of the systems such as generators, transmission lines, electric machineries and flexible ac transmission (FACTS) devices can be mathematically modelled. The EMT type programs is universally the accepted approach to analyze these subsystems and components including non-linear and switching phenomena. However, modeling and simulation of an entire bulk power system in EMT domain is computationally expensive since the time frame of interest is typically within the electromechanical transients. Therefore, the large-scale power systems' dynamic responses and transient stability are often analyzed by the fundamental frequency phasor approach, which assumes a periodic steady-state approximation because the

phasor approximations reduces the steady-state dynamics to algebraic harmonic balancing equations.

The dynamic phasor concept is an advanced approach compared to the traditional phasor representation which can capture wider bandwidth of transients. The dynamic phasor approach can also be applied to the electromagnetic transient analysis with larger time step and can be faster than the conventional time domain EMT approach. Simple examples are presented in the following sections to explain the advantages of dynamic phasor approach.

2.2.1 ABC Three-Phase Representation

The sinusoidal voltage sources in *abc* phase coordinates in time domain are represented as

$$v_i(t) = V_m \cos(\omega_0 t + \theta_i)\,,\ i = a, b, c, \tag{1}$$

where V_m is the magnitude, θ_i is the phase angle and ω_0 is the fundamental angular frequency. frequency in rad/sec. In balanced three-phase power systems, the phases are evenly displaced by 120 degrees. The positive sequence variables of symmetrical components [36] are

$$f_{p,abc} = F_p \begin{bmatrix} \cos(\omega_0 t + \theta_p) \\ \cos(\omega_0 t + \theta_p - 2\pi/3) \\ \cos(\omega_0 t + \theta_p + 2\pi/3) \end{bmatrix}. \tag{2}$$

Here, f can represent any variables such as voltage, current and flux linkage. Based on the symmetrical components theory, an unbalanced *n*-phase system can be analyzed by a balanced *n*-phase system, referred as a positive sequence, and a negative and a zero sequence components which are expressed as

$$f_{n,abc} = F_n \begin{bmatrix} \cos(\omega_0 t + \theta_n) \\ \cos(\omega_0 t + \theta_n + 2\pi/3) \\ \cos(\omega_0 t + \theta_n - 2\pi/3) \end{bmatrix} \quad (3)$$

$$f_{z,abc} = F_z \begin{bmatrix} \cos(\omega_0 t + \theta_z) \\ \cos(\omega_0 t + \theta_z) \\ \cos(\omega_0 t + \theta_z) \end{bmatrix}. \quad (4)$$

The three sets (2), (3) and (4) now can represent a balanced or unbalanced three-phase power system as

$$f_{abc}(t) = f_{p,abc} + f_{n,abc} + f_{z,abc}. \quad (5)$$

According to convention, the positive sequence components rotate in counter-clockwise (CCW) direction which is in-phase with the system frequency. The negative sequence components rotate in opposite clockwise (CW) direction. The zero sequence components have the same magnitude and phase.

For the purpose of comparison of modeling efficiencies, a balanced three-phase system composed of a series *RL* circuit without inductive coupling effect shown in Figure 2.2 is considered. This circuit can be described in time-domain by the following state-space equations:

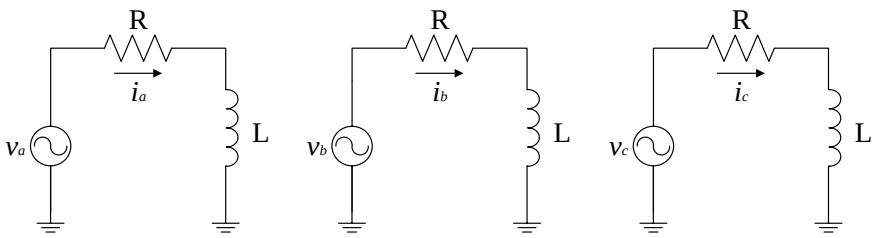

Figure 2.2 Three phase voltage in time domain.

$$L\frac{d}{dt}i_a = v_a - Ri_a$$

$$L\frac{d}{dt}i_b = v_b - Ri_b \qquad (6)$$

$$L\frac{d}{dt}i_c = v_c - Ri_c.$$

Without loss of generality, for the considered example it is assumed that L=0.1H, R=1Ω and V_t= 50V at 60 Hz. At t = 0.2s, the voltage source is applied to the circuit. Then, at t = 0.7s, a 50% voltage dip duration of six electrical cycles is applied. The resulting transient observed in inductor current in time-domain is depicted in Figure 2.3.

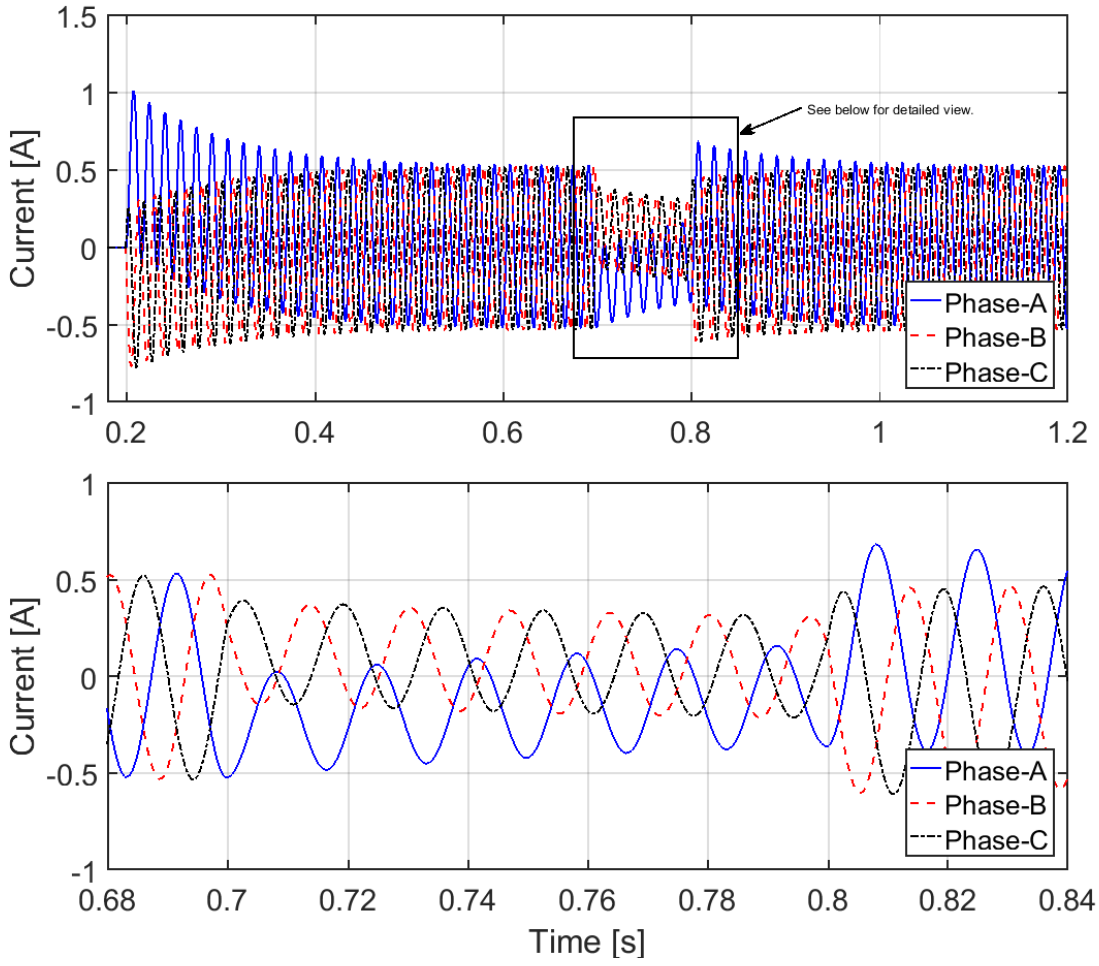

Figure 2.3 Inductor current trajectory after a 50% voltage dip for 6 cycles.

One of the advantages of *abc* three-phase representation is that any electrical equipment including machines and power electronics can be modeled in a straightforward manner using state equations similar to (6). This representation allows to capture the EMT level dynamics fairly accurately. However, the most obvious down side of using this representation is that the alternating waveform requires solution of differential equations and the use of fairly small time steps [39].

2.2.2 DQ0 Representation

The main idea of DQ0 representation is to reduce complexity of *abc* three-phase time domain models using Park's transformation [40]. This approach is widely used in the analysis of electric machinery as it eliminates time-varying inductances. The transformation is described [41] as

$$\begin{bmatrix} f_d \\ f_q \\ f_0 \end{bmatrix} = \frac{2}{3}\begin{bmatrix} \cos\theta & \cos(\theta - 2/3\pi) & \cos(\theta + 2/3\pi) \\ -\sin\theta & -\sin(\theta - 2/3\pi) & -\sin(\theta + 2/3\pi) \\ 1/2 & 1/2 & 1/2 \end{bmatrix} \cdot \begin{bmatrix} f_a \\ f_b \\ f_c \end{bmatrix}. \tag{7}$$

The inverse transform is

$$\begin{bmatrix} f_a \\ f_b \\ f_c \end{bmatrix} = \begin{bmatrix} \cos\theta & -\sin\theta & 1 \\ \cos(\theta - 2/3\pi) & -\sin(\theta - 2/3\pi) & 1 \\ \cos(\theta + 2/3\pi) & -\sin(\theta + 2/3\pi) & 1 \end{bmatrix} \cdot \begin{bmatrix} f_d \\ f_q \\ f_0 \end{bmatrix}, \tag{8}$$

where the angular displacement $\theta = \int \omega \ dt$. In general, the angular velocity ω can be arbitrary (i.e. arbitrary reference frame [43]. For the purpose of this thesis, the rotating speed of the reference frame is chosen to be the synchronous speed ω_s of the system. Then, the DQ0

synchronous reference frame rotates with the same speed as the system frequency. After applying the DQ0 transformation to (6), it becomes

$$L\frac{d}{dt}i_d = v_d - Ri_d + \omega_s L\, i_q$$

$$L\frac{d}{dt}i_q = v_q - Ri_q - \omega_s L\, i_d \tag{9}$$

$$L\frac{d}{dt}i_0 = v_0 - Ri_0.$$

The sequence component theory can also applied to DQ0 representation given as

$$f_{dq0}(t) = f_{p,dq0} + f_{n,dq0} + f_{z,dq0} \tag{10}$$

$$f_{p,dq0} = F_p \begin{bmatrix} \cos\theta_p \\ \sin\theta_p \\ 0 \end{bmatrix} \tag{11}$$

$$f_{n,dq0} = F_n \begin{bmatrix} \cos(2\omega_0 t + \theta_n) \\ -\sin(2\omega_0 t + \theta_n) \\ 0 \end{bmatrix} \tag{12}$$

$$f_{z,dq0} = F_z \begin{bmatrix} 0 \\ 0 \\ \cos(\omega_0 t + \theta_z) \end{bmatrix} \tag{13}$$

Compared to the sequence components of *abc*-phase representation, the most distinctive change is that the positive sequence components of DQ0 representation is constant value. During the steady state or balanced system, only positive sequence components are activated which makes it possible to use larger time step size. However, for unbalanced system conditions, the double frequency term of the negative sequence components in (12) creates oscillation as shown in

Figure 2.4, and the computational advantage no longer exists. In the study depicted in Figure 2.4, a balanced operation of three-phase sources is assumed. At t = 0.7s, a 50% voltage dip is applied to *a*-phase terminal of the same circuit in Figure 2.2 for six electrical cycles, which due to the term in negative sequence components results in double frequency (i.e.12 cycles oscillation) in *d* and *q* component and fundamental frequency (i.e. 6 cycles oscillation) in *0* component, as seen in Figure 2.4.

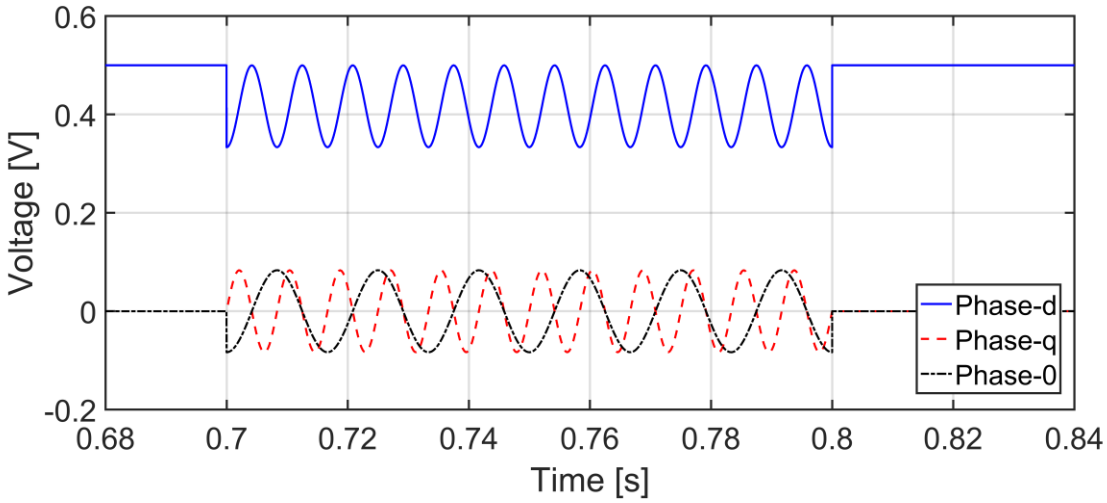

Figure 2.4 Trajectory of voltage in *dq0* synchronous reference frame during an unbalanced voltage dip (Phase A 50%).

2.2.3 Dynamic Phasor Representation

When analyzing large-scale transient stability where fast transient such as EMT is neglected, it is common to assume that voltages and currents are periodic sinusoidal and can be modeled by phasors. It is also assumed that the power system is balanced and its operation is centered on the fundamental system frequency 50/60 Hz. These assumptions are referred to as the quasi-steady state approach. This the quasi-steady phasor representation of sinusoidal signals has significant advantages especially for analyzing a steady state or very slow electromechanical phenomenon.

However, during fast balanced and unbalanced disturbances, the assumption of pure periodic sinusoidal signals at fixed frequency may not be valid. Thus this quasi-steady phasor approach will lose its accuracy for analysis of fast transients.

Dynamic phasor approach was introduced in 1991 [20] and can address different frequency components separately. The concept of dynamic phasor is originated from the Fourier series concept [42]. Specifically, a periodic signal, $x(\tau) = x(\tau + T)$, with period T, can be represented as

$$x(\tau) = \sum_{k=-\infty}^{\infty} X_k \cdot e^{j\frac{2\pi k}{T}\tau}, \tag{14}$$

where $\frac{2\pi}{T}$ is angular velocity. The Fourier coefficient X_k is time invariant and defined as

$$X_k = \frac{1}{T}\int_0^T x(\tau) \cdot e^{-j\frac{2\pi k}{T}\tau} d\tau. \tag{15}$$

If a quasi-periodic signal $x(\tau)$ is approximated within the interval $\tau \in (t - T, t]$, the Fourier series (14) can be re-written as

$$x(\tau) = \sum_{k=-\infty}^{\infty} X_k(t) \cdot e^{j\frac{2\pi k}{T}\tau}, \tag{16}$$

where the Fourier coefficient $X_k(t)$ is now time varying as the integral interval varies with time.

The time variant Fourier coefficient is defined as a dynamic phasor (DP) as following

$$X_k(t) = \frac{1}{T}\int_{t-T}^{t} x(\tau) \cdot e^{-jk\omega_s\tau} d\tau = \langle x \rangle_k(t), \tag{17}$$

where k is the DP index.

Based on DP approach, the original quasi-periodic signal $x(t)$ is derived from a number of selected sets of dynamic phasors as

$$x(t) \cong \sum_{k \in K} X_k(t) \cdot e^{jk\omega_s t}, \tag{18}$$

where *K* is the set of DP index selected to approximate the original signal. The more DP terms are included, the more accurate the result will be, which will come increasing computational expense. Therefore, choosing appropriate sets of DPs is directly related to the efficiency of modeling.

There are three major characteristics of DP as below;

1) Derivatives of time-domain

$$\langle \frac{dx}{dt} \rangle_k = \frac{d\langle x \rangle_k}{dt} + jk\omega_s \langle x \rangle_k \tag{19}$$

2) Product of two time-domain variables $x(t)$ and $y(t)$

$$\langle xy \rangle_k = \sum_{l=-\infty}^{\infty} (\langle x \rangle_{k-l} \langle y \rangle_l) \tag{20}$$

3) Conjugate property for a real value time-domain signal

$$\langle x \rangle_k^* = \left(\frac{1}{T} \int_{t-T}^{t} x(t) \cdot e^{-jk\omega_s t} dt \right)^* = \frac{1}{T} \int_{t-T}^{t} x(t) \cdot e^{jk\omega_s t} dt = \langle x \rangle_{-k} \tag{21}$$

Based on above DP properties, the simple series *RL* circuit derived in (6) can be written in DP domain as follows:

$$L\frac{d}{dt}\langle i\rangle_k = \langle v\rangle_k - R\langle i\rangle_k - jk\omega_s\langle i\rangle_k, \tag{22}$$

where *k* refers to the k^{th} Fourier coefficient of current. Since the considered *abc* system in time-domain system is considered balanced, only *a*-phase equation is described, as the other two phases has exactly the same with appropriate phase shifts by 120 degrees.

The DP $\langle i\rangle_k$ is a complex number which has its real and imaginary components as

$$\langle i\rangle_k = i_k^R + ji_k^I, \tag{23}$$

where the super-scripts *R* and *I* denote the real and imaginary components, respectively. Then, (22) can be written as two separate equations for real and imaginary components as

$$\begin{aligned} L\frac{d}{dt}i_k^R &= v_k^R - Ri_k^R + k\omega_s i_k^I \\ L\frac{d}{dt}i_k^I &= v_k^I - Ri_k^I - k\omega_s i_k^R \end{aligned} \tag{24}$$

Since the source is assumed to be ideal sinusoidal voltage source, only the fundamental frequency component is considered to approximate the original time-domain signal. Therefore, the final DP model equation becomes

$$\begin{aligned} L\frac{d}{dt}i_k^R &= v_k^R - Ri_k^R + \omega_s i_k^I \\ L\frac{d}{dt}i_k^I &= v_k^I - Ri_k^I - \omega_s i_k^R \end{aligned} \tag{25}$$

The magnitude of DP is calculated by

$$|\langle i\rangle_1| = \sqrt{(i_1^R)^2 + (i_1^I)^2}. \tag{26}$$

For the purpose of illustration, the same circuit in Figure 2.2 and operation condition in section 2.2.1 are considered in DP domain. The real and imaginary parts of DP signal is depicted in Figure 2.5, and the DP magnitude is compared to the result of time-domain model in Figure 2.6. As expected and can be seen in Figure 2.5, the trajectory of real and imaginary component of DP has the fundamental frequency oscillation during the transient and DC value when the system reaches the steady state. Also, it is noted that the magnitude of DP follows the envelope of the original time-domain signal.

Finally, the time domain signal can be reconstructed from the DP based on (18) as

$$i(t) \cong \sum_{k \in K} i_k(t) \cdot e^{jk\omega_s t} = Re\{i_1(t) \cdot e^{j\omega_s t}\}. \tag{27}$$

Figure 2.7 shows that the signal converted from the DP-domain is very accurate and almost the same as the original EMT time-domain signal.

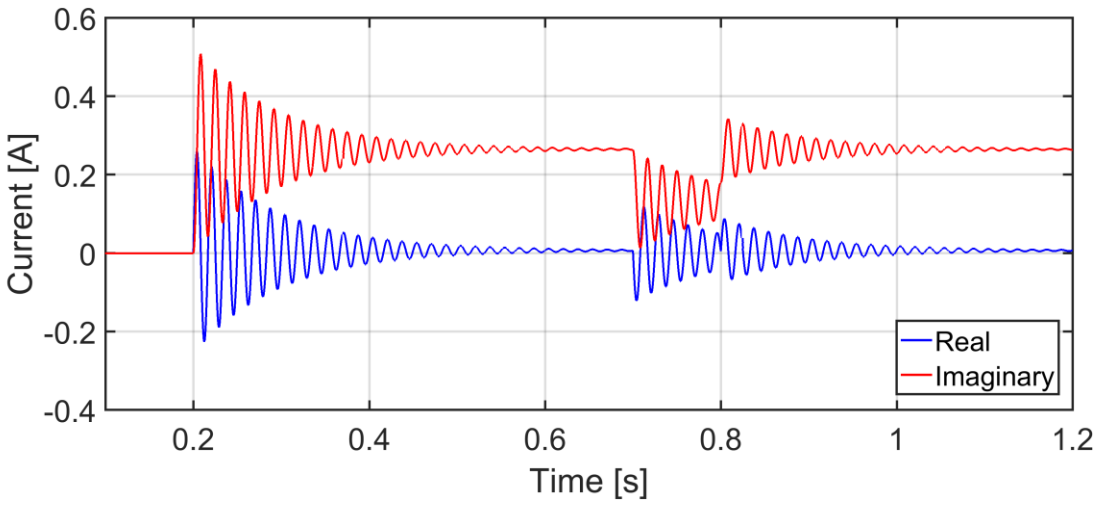

Figure 2.5 Trajectory of dynamic phasor real and imaginary component.

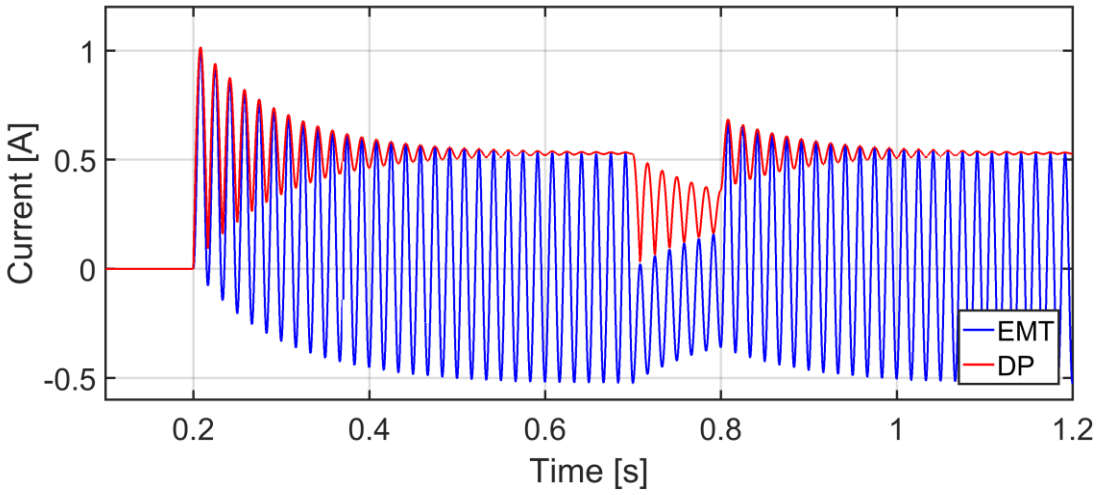

Figure 2.6 Comparison of DP magnitude and EMT signal.

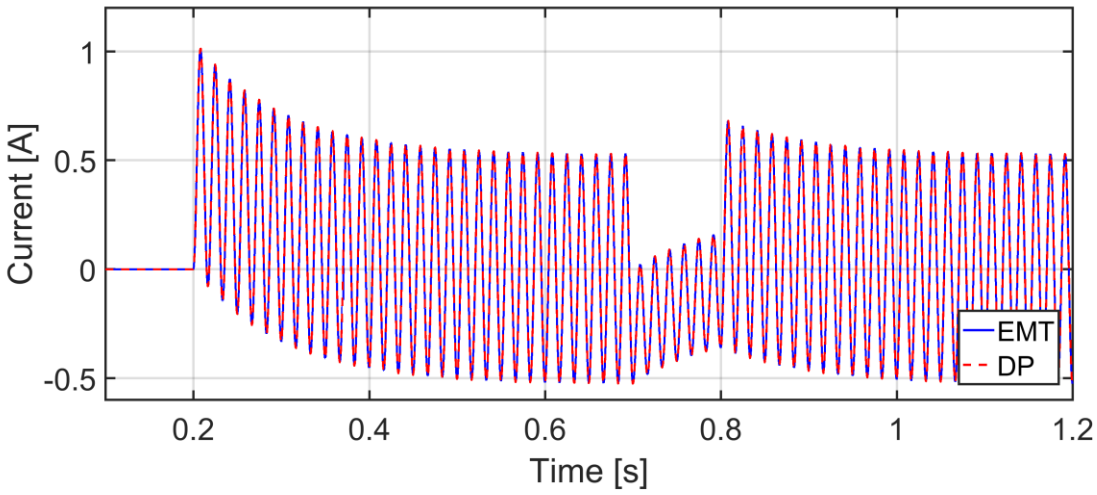

Figure 2.7 Comparison of DP and EMT signal in time-domain.

2.3 Chapter Summary

In this chapter, the power system dynamics were briefly reviewed and different modeling techniques were demonstrated by analyzing an example of series *RL* circuit. The main interests of this chapter is to see what modeling techniques should be chosen depending on the time frame of interest and the system dynamics. The advantages and disadvantages of representation in *abc*-phase coordinates, transformed DQ0-coordinates, and DP approaches have been presented. Throughout the analysis of considered example, it can be concluded that the DP approach is accurate and can be numerically efficient for representing the slower transients.

Chapter 3: Modeling of DFIG

In this chapter, the fundamental theory and principles of the DFIG model are presented. The detail reference model in time-domain (i.e. the EMT Model) is developed, and the proposed full-order dynamic phasor model (i.e. the DP Model) and the reduced-order dynamic phasor model (i.e. the DP-ROM) are derived, respectively.

3.1 Space Vector Representation

The space-vector approach can compactly represent the three-phase variables as one rotating vector, which makes it possible to derive the differential equations of DFIG in a simpler way [43]. Under the assumption of balanced three-phase system, the voltage source is

$$\begin{bmatrix} v_a \\ v_b \\ v_c \end{bmatrix} = V_m \begin{bmatrix} \cos(\omega_s t + \theta) \\ \cos(\omega_s t + \theta - 2\pi/3) \\ \cos(\omega_s t + \theta + 2\pi/3) \end{bmatrix}, \tag{28}$$

where V_m is the voltage magnitude, ω_s is the system fundamental frequency.

This balanced three-phase voltage source can be represented as one space-vector that rotates at angular speed as ω_s. The stationary *abc*-phase axes of the plane are defined as (29) and a voltage vector $\vec{V}$ can be represented in *abc*-axes as depicted in Figure 3.1 (a).

$$\begin{aligned} \vec{a} &= 1 \\ \vec{b} &= e^{j(\frac{2\pi}{3})} \\ \vec{c} &= e^{j(\frac{4\pi}{3})}. \end{aligned} \tag{29}$$

The rotating voltage vector is represented as

$$\vec{v} = |\vec{v}|e^{j(\omega_s t+\theta)}. \tag{30}$$

This voltage vector can be represented alternatively by two variables, v_α and v_β, in the $\alpha\beta$-complex plane depicted in Figure 3.1 (b) and written as

$$\vec{v} = v_\alpha + jv_\beta = \frac{2}{3}\left(v_a + v_b e^{\frac{j2\pi}{3}} + v_c e^{-\frac{j2\pi}{3}}\right)$$

$$v_\alpha = Re\{\vec{v}\} = \frac{2}{3}\left(v_a - \frac{1}{2}v_b - \frac{1}{2}v_c\right) \tag{31}$$

$$v_\beta = Im\{\vec{v}\} = \frac{1}{\sqrt{3}}(v_b - v_c).$$

The transformation from three-phase to two-phase complex plane is equivalent to the Clarke's transformation in matrix form:

$$\begin{bmatrix} v_\alpha \\ v_\beta \end{bmatrix} = \frac{2}{3}\begin{bmatrix} 1 & -\frac{1}{2} & -\frac{1}{2} \\ 0 & \frac{\sqrt{3}}{2} & -\frac{\sqrt{3}}{2} \end{bmatrix} \cdot \begin{bmatrix} v_a \\ v_b \\ v_c \end{bmatrix}, \tag{32}$$

where the constant 2/3 is chosen for the magnitude of voltage vector to be the same as the peak value of the three phase voltages.

Note that v_α, v_β, v_a, v_b, and v_c are not constant value in the *abc* and $\alpha\beta$ stationary reference frame and the voltage vector is rotating at the synchronous speed ω_s. If there is an arbitrary reference frame rotating in synchronous speed, then the magnitude of each phase will be constant value which is commonly referred to as a *dq* synchronous reference frame as shown in Figure 3.1 (c).

For transformation from $\alpha\beta$ stationary reference to dq synchronous reference frame, the following equation is used:

$$\vec{v}^{s} = \begin{bmatrix} v_d \\ v_q \end{bmatrix} = \begin{bmatrix} \cos(\theta_s) & -\sin(\theta_s) \\ \sin(\theta_s) & \cos(\theta_s) \end{bmatrix} \cdot \begin{bmatrix} v_\alpha \\ v_\beta \end{bmatrix}, \tag{33}$$

$$\vec{v}^{s} = e^{-j\theta_s}\vec{v}^{\alpha}, \tag{34}$$

where the superscript of voltage vector 'α' and 's' denotes that the voltage vector is referred to the stationary and synchronous reference frame, respectively.

In summary, space vector approach has the same result as the Park's transformation and it gives more intuitive procedures.

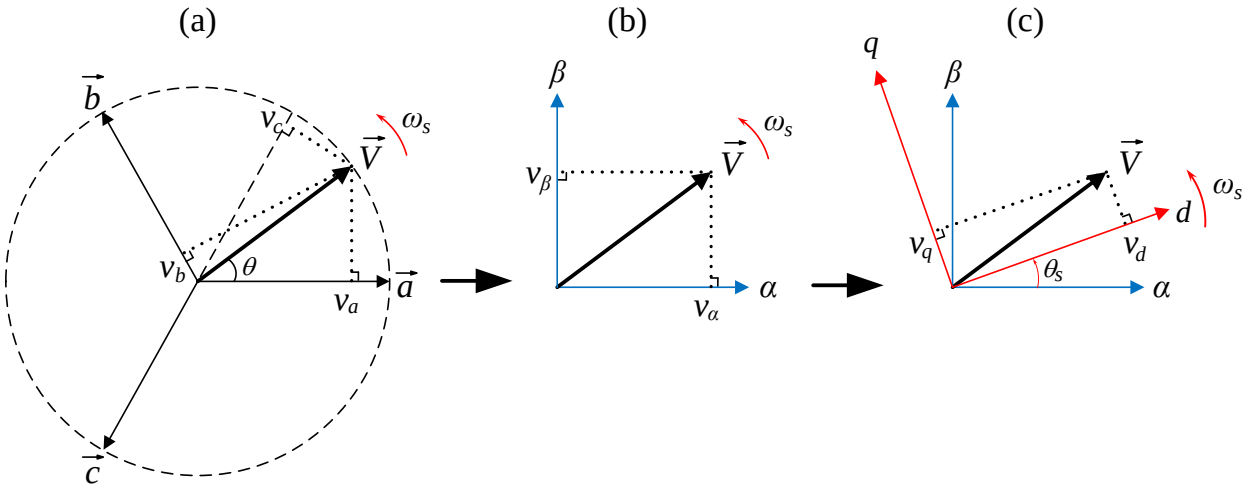

Figure 3.1 Space vector representation of the same voltage vector in *abc*, *αβ* and *dq* reference frame.

3.2 Wound Rotor Induction Generator (WRIG)

In this section, the state-space model of WRIG [4][41][43] will be derived based on the space-vector approach with following assumptions:

1) An ideal symmetrical machine with sinusoidally distributed windings and MMF is considered; therefore, the effect of teeth and slots is neglected.
2) Saturation, hysteresis loss, and eddy loss are neglected.
3) All parameters of rotor side are referred to stator side.
4) All model components are developed in per-unit.
5) The WRIG model is assumed to be in *dq* synchronous reference frame where the stator voltage space vector is aligned with *d*-axis.

3.2.1 Wound Rotor Induction Generator in Time-domain Representation

The three-phase coupled stator and rotor circuit is depicted in Figure 3.2. The corresponding stator and rotor voltage equations in *abc*-phase variables and coordinates are

$$v_{as}(t) = R_s i_{as}(t) + \frac{d\psi_{as}(t)}{dt} \tag{35}$$

$$v_{bs}(t) = R_s i_{bs}(t) + \frac{d\psi_{bs}(t)}{dt} \tag{36}$$

$$v_{cs}(t) = R_s i_{cs}(t) + \frac{d\psi_{cs}(t)}{dt}. \tag{37}$$

$$v_{ar}(t) = R_r i_{ar}(t) + \frac{d\psi_{ar}(t)}{dt} \tag{38}$$

$$v_{br}(t) = R_r i_{br}(t) + \frac{d\psi_{br}(t)}{dt} \tag{39}$$

$$v_{cr}(t) = R_r i_{cr}(t) + \frac{d\psi_{cr}(t)}{dt}. \tag{40}$$

Equations (35)-(40) describe the coupled-circuit model which has time-variant inductances and fluxes. In order to eliminate the time dependent term in mutual inductances, the time domain representation is transformed to the synchronous reference frame in space-vector representation.

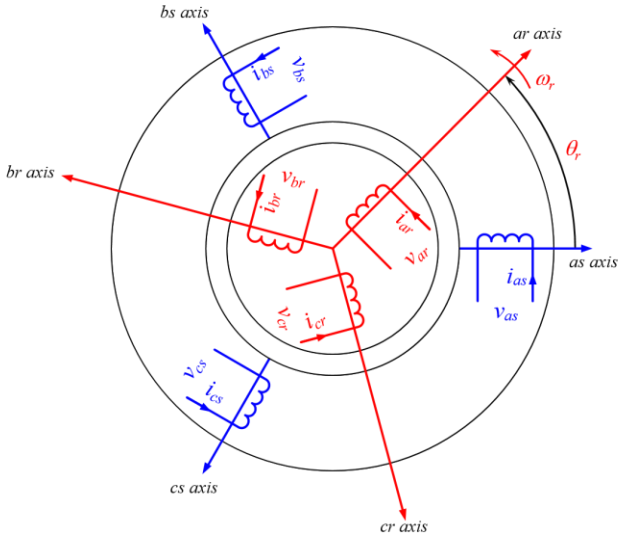

Figure 3.2 Three-phase symmetrical induction machine.

3.2.2 Wound Rotor Induction Generator in Space Vector Representation

Using the space-vector properties (29) – (31), the stator circuit equations can be rewritten as one space-vector in $\alpha\beta$ stationary reference frame as depicted in Figure 3.1,

$$\vec{v}_s^{\alpha} = R_s \vec{i}_s^{\alpha} + \frac{d\vec{\psi}_s^{\alpha}}{dt} \tag{41}$$

where superscript letter 'α' indicates that the stator side vectors are in $\alpha\beta$ stationary reference frame and subscript letter 's' denotes stator circuit. Similarly, the rotor circuit equation can be written as

$$\vec{v}_r^{r} = R_r \vec{i}_r^{r} + \frac{d\vec{\psi}_r^{r}}{dt}, \tag{42}$$

where superscript letter ‘r’ indicates that the rotor side vectors are in *DQ* rotor reference frame and subscript letter ‘r’ denotes rotor circuit.

Next step is to transform vectors (41) and (42) to the synchronous reference frame based on Figure 3.2. Considering that the angle between α-axis and *d*-axis is θ_s, and the angle between *d*-axis and *D*-axis is θ_r, (41) and (42) can be transformed to synchronous reference frame, multiplying them by $e^{-j\theta_s}$ and $e^{-j\theta_r}$, respectively. The final equations in synchronous reference frame are

$$\overrightarrow{v_s} = R_s\overrightarrow{\imath_s} + \frac{d\overrightarrow{\psi_s}}{dt} + j\omega_s\overrightarrow{\psi_s}, \tag{43}$$

$$\overrightarrow{v_r} = R_r\overrightarrow{\imath_r} + \frac{d\overrightarrow{\psi_r}}{dt} + j(\omega_s - \omega_r)\overrightarrow{\psi_r}, \tag{44}$$

where ω_r is the rotor electrical angular speed, and the angular slip frequency is defined as

$$\omega_{sl} = \omega_s - \omega_r. \tag{45}$$

For simplicity of notations, the vectors without superscript letter indicate that the synchronous reference frame which is base reference frame for the final DFIG model. The flux equations in synchronous reference frame are expressed as

$$\overrightarrow{\psi_s} = L_s\overrightarrow{\imath_s} + L_m\overrightarrow{\imath_r}, \tag{46}$$

$$\overrightarrow{\psi_r} = L_m\overrightarrow{\imath_s} + L_r\overrightarrow{\imath_r}. \tag{47}$$

Here, L_s and L_r are the stator and rotor self-inductances defined as

$$L_s = L_m + L_{ls}, \tag{48}$$

$$L_r = L_m + L_{lr}, \tag{49}$$

where L_m, L_{ls} and L_{lr} are the magnetizing inductance, and stator and rotor leakage inductances, respectively. Unlike the time-domain coupled-circuit model in *abc*-coordinates, the transformed variables in synchronous reference frame are constant in steady state.

Note that machine and power system parameters are usually given in per-unit. Therefore, it is convenient to use all models in per-unit. The model in per-unit can be derived based on the relation between base voltage and flux as

$$V_b = \omega_b \psi_b, \tag{50}$$

where v_b, ω_b and ψ_b are base voltage, angular frequency and flux linkage. Equation (43) and (44) can be re-written as

$$\frac{\overrightarrow{v_s}}{V_b} = \frac{R_s \overrightarrow{\imath_s}}{Z_b I_b} + \frac{1}{\omega_b \psi_b} \frac{d\overrightarrow{\psi_s}}{dt} + \frac{j\omega_s}{\omega_b} \frac{\overrightarrow{\psi_s}}{\psi_b} \tag{51}$$

$$\frac{\overrightarrow{v_r}}{V_b} = \frac{R_r \overrightarrow{\imath_r}}{Z_b I_b} + \frac{1}{\omega_b \psi_b} \frac{d\overrightarrow{\psi_r}}{dt} + j\frac{(\omega_s - \omega_r)}{\omega_b} \frac{\overrightarrow{\psi_r}}{\psi_b}. \tag{52}$$

The final per-unit wound rotor induction machine model for computer studies can be written as:

$$\frac{1}{\omega_b} \frac{d}{dt} \begin{bmatrix} \psi_{ds} \\ \psi_{qs} \end{bmatrix} = \begin{bmatrix} v_{ds} \\ v_{qs} \end{bmatrix} - R_s \begin{bmatrix} i_{ds} \\ i_{qs} \end{bmatrix} - \omega_s \begin{bmatrix} 0 & -1 \\ 1 & 0 \end{bmatrix} \begin{bmatrix} \psi_{ds} \\ \psi_{qs} \end{bmatrix} \tag{53}$$

$$\frac{1}{\omega_b} \frac{d}{dt} \begin{bmatrix} \psi_{dr} \\ \psi_{qr} \end{bmatrix} = \begin{bmatrix} v_{dr} \\ v_{qr} \end{bmatrix} - R_s \begin{bmatrix} i_{dr} \\ i_{qr} \end{bmatrix} - \omega_{sl} \begin{bmatrix} 0 & -1 \\ 1 & 0 \end{bmatrix} \begin{bmatrix} \psi_{dr} \\ \psi_{qr} \end{bmatrix} \tag{54}$$

$$\begin{bmatrix} \psi_{ds} \\ \psi_{qs} \\ \psi_{dr} \\ \psi_{qr} \end{bmatrix} = \begin{bmatrix} X_s & 0 & X_m & 0 \\ 0 & X_s & 0 & X_m \\ X_m & 0 & X_r & 0 \\ 0 & X_m & 0 & X_r \end{bmatrix} \begin{bmatrix} i_{ds} \\ i_{qs} \\ i_{dr} \\ i_{qr} \end{bmatrix} \tag{55}$$

The mechanical system is considered as a single rigid mass system, for which the speed is expressed as

$$\frac{d}{dt}\omega_r = \frac{T_e - T_m}{2H}, \tag{56}$$

where T_e, T_m and H are electromagnetic torque, mechanical torque, and inertia constant, respectively. Equations (53) – (56) define the final 5th order WRIG model. The electrical torque, active, and reactive powers are calculated as following:

$$T_e = X_m\left(i_{qs}i_{dr} + i_{ds}i_{qr}\right) = \psi_{qr}i_{dr} + \psi_{dr}i_{qr} \tag{57}$$

$$P_s = \frac{3}{2}Re\left\{\overrightarrow{v_s}\cdot\overrightarrow{i_s}^*\right\} = \frac{3}{2}\left(v_{ds}i_{ds} + v_{qs}i_{qs}\right) \tag{58}$$

$$P_r = \frac{3}{2}Re\left\{\overrightarrow{v_r}\cdot\overrightarrow{i_r}^*\right\} = \frac{3}{2}\left(v_{dr}i_{dr} + v_{qr}i_{qr}\right) \tag{59}$$

$$Q_s = \frac{3}{2}Im\left\{\overrightarrow{v_s}\cdot\overrightarrow{i_s}^*\right\} = \frac{3}{2}\left(v_{qs}i_{ds} - v_{ds}i_{qs}\right) \tag{60}$$

$$Q_r = \frac{3}{2}Im\left\{\overrightarrow{v_r}\cdot\overrightarrow{i_r}^*\right\} = \frac{3}{2}\left(v_{qr}i_{dr} - v_{dr}i_{qr}\right). \tag{61}$$

3.3 Wind Turbine

In this section, a commonly used wind turbine model with MPPT control is presented. The mechanical power P_m generated by a wind turbine is related to the power coefficient C_P and kinetic power P_{wind} based on the following equation [44]:

$$P_m = C_P \cdot P_{wind}. \tag{62}$$

The kinetic power P_{wind} of wind is defined as

$$P_{wind} = \frac{1}{2}\rho A v_w^3, \tag{63}$$

where $A = \pi R^2$ is the surface of the wind blade of radius R, and v_w is the average wind speed measured at the height of the wind turbine. Equation (62) and (63) are general characteristics of wind turbines. The power coefficient C_P is the function of tip speed ratio λ and pitch angle β expressed as

$$C_P(\lambda, \beta) = c_1 \left(c_2 \frac{1}{\Lambda} - c_3 \beta - c_4 \beta^{c_5} - c_6 \right) e^{-c_7 \frac{1}{\Lambda}},$$
$$\lambda = \frac{\omega_t R}{v_w}, \frac{1}{\Lambda} = \frac{1}{\lambda + c_8 \beta} - \frac{c_9}{1 + \beta^3}, \tag{64}$$

where the coefficients c_1 to c_9 are defined for a specific wind turbine characteristic and parameters, and ω_t is the blade angular velocity. The characteristic parameters used in this thesis correspond to the MATLAB/Simulink built-in model summarized in Appendix A.1.

The final turbine power characteristics curve with zero pitch angle and parameters in Appendix A.1 is shown in Figure 3.3. The pitch angle is controlled by pitch controller which is designed to control the angle of attack of the blades against the wind. The purpose of the pitch control system is to optimize the turbine output power at its designed range when the wind speed is below its rated speed [4].

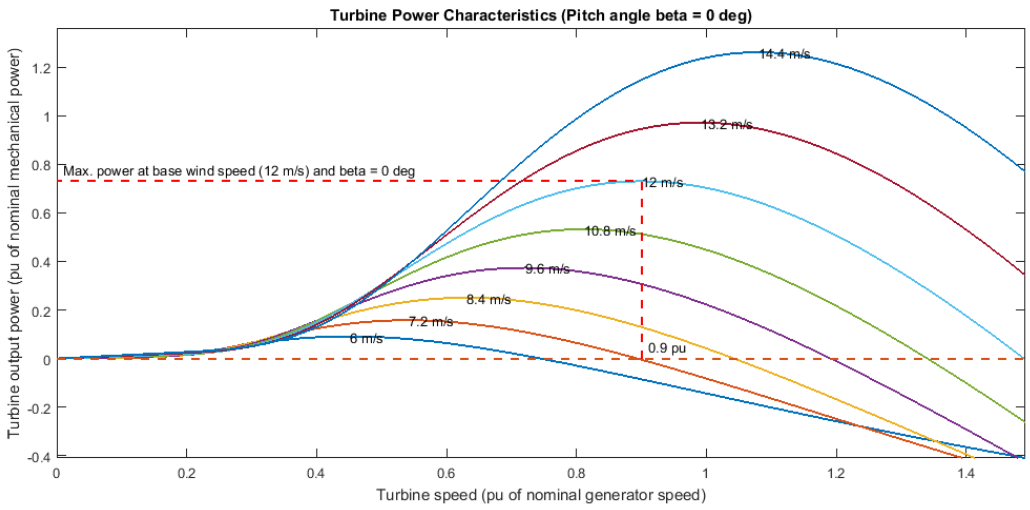

Figure 3.3 Wind turbine power characteristics curve [45]**.**

3.3.1 Maximum Power Point Tracking (MPPT)

The main purpose of MPPT control scheme is to capture maximum wind power at different wind speed by controlling the turbine speed to optimize the tip speed ratio at its desired level [4][6]. As shown in Figure 3.3, there are different maximum power point at different wind speeds.

The turbine's maximum output power is captured when the power coefficient is at its maximum value, denoted by $C_{P_{max}}$. This operation is achieved by matching the generator electrical torque with $k_P {\omega_t}^2$ [6]. The parameter k_P is calculated based on the characteristics parameters c_1 to c_9 as

$$k_P = \frac{1}{2}\left(\frac{c_1 c_2}{c_7}\right) e^{-\frac{c_6 c_7}{c_2}-1} \rho \mathrm{A} \frac{R^3}{\left(\frac{c_2 c_7}{c_2 c_9 c_7 + c_6 c_7 + c_2}\right)^3}. \quad (65)$$

For this thesis, based on the given characteristics parameters, the k_P is calculated to be 0.73. The final optimal power point is calculated as

$$P_{MPPT} = k_P \omega_t{}^3. \tag{66}$$

In per-unit system, the turbine speed ω_t and the rotor speed ω_r are equal; therefore, the gearbox ratio is not used in the per-unit model. Then, the rotor speed is used to obtain the reference power point in MPPT control, which is proportional to the cube of rotor speed.

3.4 Controllers

In this section, a mathematical model of DFIG controller is derived based on the vector control approach [4][46]. The controller assumes a constant DC link voltage in back-to-back converter shown in Figure 3.4.

The objective of RSC is to control the output active and reactive power, whereas the objective of GSC is to keep the DC link voltage as constant and supply reactive power to the grid. Based on the configuration shown in Figure 3.4, the DC link dynamics is expressed as

$$\frac{1}{\omega_s}\frac{dv_{DC}}{dt} = \frac{1}{C}\left(\frac{P_r - P_g}{v_{DC}}\right) \tag{67}$$

If the DC link voltage is assumed constant, then (64) represents the power balance between the rotor and grid side. Therefore, a simplified controller for DFIG can be obtained by omitting the GSC controller as depicted in Figure 3.5. It is reasonable to assume that the DC-link voltage is always within certain operating range to ensure the continuous operation of the RSC. This

assumption is considered sufficient for modelling the DFIG for the transient stability studies. In addition, modern DFIGs utilize additional DC-chopper circuit to limit the DC-link voltage during abnormal operation and grid disturbances [10][43].

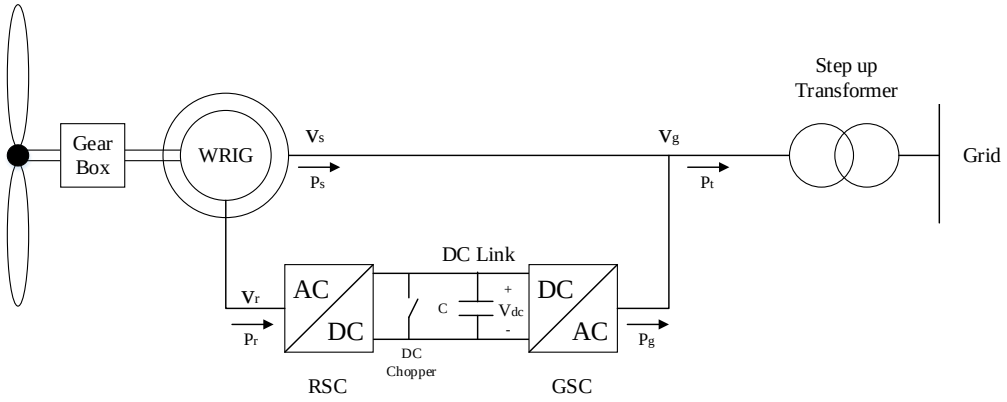

Figure 3.4 Typical DFIG with back-to-back converter composed of RSC and GSC.

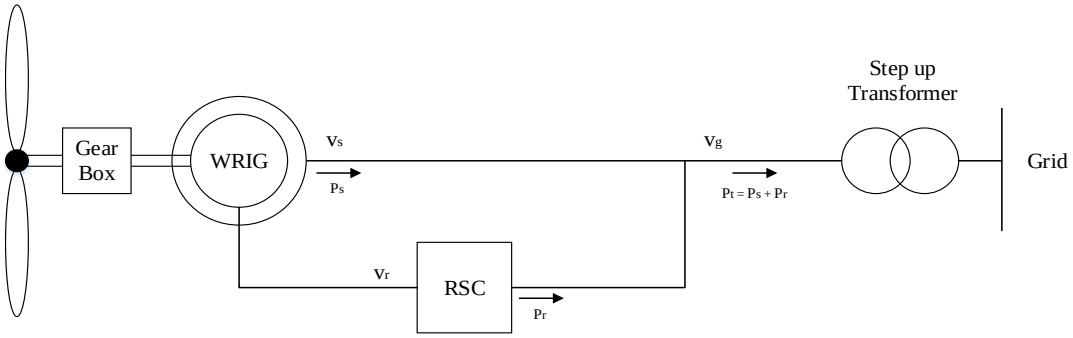

Figure 3.5 A simplified controller configuration for transient stability studies.

3.4.1 Vector Control Approach

Control of electric machinery is directly related to the electromagnetic torque of the machine. Unlike DC machines, fluxes and currents in AC machines are coupled, which makes it difficult to control. The vector control has been derived to make the AC machines to behave like DC machines in terms of torque control. The basic idea of vector control principle is to separate the

portion of current related to magnetization of the machine and torque production in a synchronously rotating *dq* synchronous reference frame.

Since DFIG's stator winding is directly connected to the grid side, the stator-voltage-oriented control (SVOC) method is commonly used as the stator voltage is easy to measure, and the frequency remain constant during normal operation [47][48].

The RSC controller is expressed in *dq* synchronous reference frame where the stator voltage space vector is aligned with the *d*-axis. The equations for the RSC are described in the following section.

3.4.2 Rotor Side Converter

3.4.2.1 Reference Current Calculation

Considering that the stator resistance is negligible, the angle difference between the stator voltage and flux is assumed to be 90 degrees, which leads to the following condition

$$\begin{aligned} \psi_{ds} &= v_{qs} = 0 \\ v_{ds} &= V_s \cong \omega_s \psi_s \end{aligned} \tag{68}$$

Based on condition (68), equation (43) is written in *dq* components as

$$\begin{aligned} \psi_s = \psi_{qs} &= i_{qs} L_s + i_{qr} L_m \\ 0 &= i_{ds} L_s + i_{dr} L_m. \end{aligned} \tag{69}$$

Then, the current equation is redefined as

$$i_{qs} = \frac{\psi_s}{L_s} - i_{qr}\frac{L_m}{L_s}$$
$$i_{ds} = -i_{dr}\frac{L_m}{L_s}. \tag{70}$$

The stator active and reactive power is expressed as

$$P_s = \frac{3}{2}(v_{ds}i_{ds}) = -\left(\frac{3}{2}\frac{L_m}{L_s}V_s\right)i_{dr} \tag{71}$$

$$Q_s = \frac{3}{2}\left(v_{ds}i_{qs}\right) = \frac{3}{2}\frac{{V_s}^2}{\omega_s L_s} - \left(\frac{3}{2}\frac{L_m}{L_s}V_s\right)i_{qr}. \tag{72}$$

Equations (71) and (72) show that a decoupled control for the real P_s and reactive Q_s power is achieved by controlling the rotor currents i_{dr} and i_{qr}. Therefore, the currents i_{dr} and i_{qr} are controlled by the outer control loop to regulate P_s and Q_s independently. Therefore, the reference current can be calculated based on (71) and (72) as

$$i_{dr} = -\frac{2L_s}{3V_s L_m}P_s \tag{73}$$

$$i_{qr} = \frac{2L_s}{3V_s L_m}Q_s - \frac{V_s}{\omega_s L_m}. \tag{74}$$

3.4.2.2 Control Loop

Since the rotor voltage dynamics determine the control loop characteristics, the relationship between the rotor voltage and current can be obtained from (41) and (44). The rotor flux and current has following relationship

$$\psi_{qr} = \sigma L_r i_{qr} + \frac{L_m}{L_s}\psi_s,$$
$$\psi_{dr} = \sigma L_r i_{dr}, \tag{75}$$

where the leakage inductance coefficient is defined as $\sigma = 1 - \frac{{L_m}^2}{L_s L_r}$. Substituting (75) into (41), the rotor voltage and current relationship can be written as

$$v_{dr} = R_r i_{dr} - \omega_r \sigma L_r i_{qr} + \sigma L_r \frac{d}{dt} i_{dr} + \frac{L_m}{L_s}\frac{d}{dt}\psi_s. \tag{76}$$

$$v_{qr} = R_r i_{qr} + \omega_r \sigma L_r i_{dr} + \sigma L_r \frac{d}{dt} i_{qr} + \omega_r \frac{L_m}{L_s}\psi_s. \tag{77}$$

In (76), the last term can be neglected as the stator flux magnitude ψ_s is constant during normal operation. The last term in (77) is not dependent of rotor current. So, this term can be neglected as the disturbance will be handled by controller. The second term in (76) and (77) is a feedforward compensation which can be also neglected as it does not affect the control loop function [43]. The plant model can be derived as a first-order transfer function as

$$i_{dr}(s) = \frac{1}{R_r + \sigma L_r s} v_{dr}(s) \tag{78}$$

$$i_{qr}(s) = \frac{1}{R_r + \sigma L_r s} v_{qr}(s). \tag{79}$$

To obtain the rotor voltage, PI controllers are implemented in the control loop based on the transfer function. The PI controller parameters are calculated analytically first and tuned via trial and error method. All parameters are summarized in the Table A.2 in Appendix A.2.

The overall RSC control block diagram is shown in

Figure 3.6. The control objective of the RSC is achieved by one set of PI controller at each axis for a decoupled control scheme.

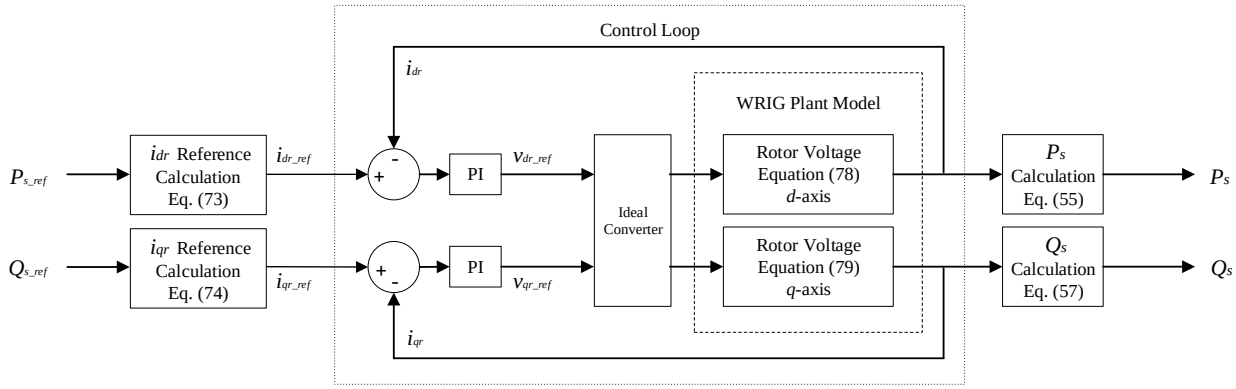

Figure 3.6 Block diagram of Vector control scheme for RSC.

For the purpose of RSC controller, an ideal converter model is considered. Therefore, the output of the controller v_{dqr} is directly fed into the WRIG rotor circuit and controls the rotor voltage. Since the DC link voltage V_{DC} is considered constant and the GSC is neglected, it follows that the rotor power P_r is delivered to the grid together with stator power P_s without losses.

3.5 Time-domain Reference EMT Model

In this section, the time-domain reference EMT model is developed based on models of each component described in previous sections. The implementation of this model is depicted in Figure 3.7. The voltage source v_{abcs}, the wind speed V_w, and the reactive power reference command Q_{s_ref} are the system inputs. The resulting currents I_{abcs} injected into the grid are the system outputs.

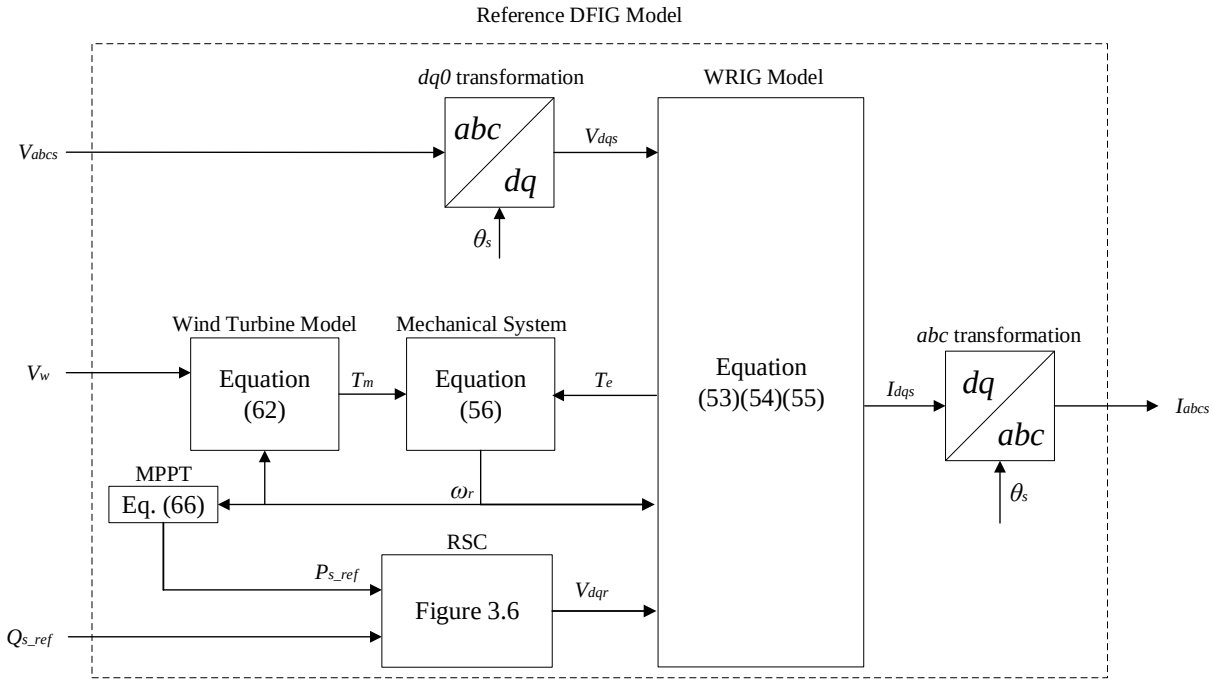

Figure 3.7 Overall Block Diagram of reference EMT Model.

3.6 Proposed DP Model

In this section, the proposed dynamic phasor model is developed based on the reference time domain model by applying the DP formulation described in (19), (20) and (21). The proposed DP Model will be tested in Chapter 4 and the results will be compared to the reference model.

3.6.1 Dynamic Phasor in Space Vector

The detailed derivation and application examples are given in [22]. Using Euler formula and space-vector theory, the three-phase DP vectors can be derived from three-phase time-domain voltage equation (28) as

$$v_i = \frac{V_i\, \mathrm{e}^{j\theta_i}\mathrm{e}^{j\omega t} + V_i \mathrm{e}^{-j\theta_i}\mathrm{e}^{-j\omega t}}{2}, \qquad i = a, b, c. \tag{80}$$

Applying the DP Conjugate property (21) and (31) to the equation (80), the three-phase DP vectors can be obtained as

$$\langle v_i \rangle_1 = \frac{1}{2} V_i \mathrm{e}^{j\theta_i}, \qquad \langle v_i \rangle_{-1} = \langle v_i \rangle_1{}^* = \frac{1}{2} V_i \mathrm{e}^{-j\theta_i}, \qquad i = a, b, c. \tag{81}$$

$$\begin{aligned} \vec{v} = \frac{2}{3} e^{j\omega t} \left\{ \langle v_a \rangle_1 + \langle v_b \rangle_1 e^{j2\pi/3} + \langle v_c \rangle_1 e^{-j2\pi/3} \right\} \\ + \frac{2}{3} e^{-j\omega t} \left\{ \langle v_a \rangle_1{}^* + \langle v_b \rangle_1{}^* e^{j2\pi/3} + \langle v_c \rangle_1{}^* e^{-j2\pi/3} \right\}. \end{aligned} \tag{82}$$

Equation (82) can be written in terms of *dq* components in synchronous reference frame as

$$\begin{aligned} \vec{v} e^{-j\omega t} = v_d + j v_q = \\ \frac{2}{3} \left\{ \langle v_a \rangle_1 + \langle v_b \rangle_1 e^{j2\pi/3} + \langle v_c \rangle_1 e^{-j2\pi/3} \right\} \\ + \frac{2}{3} e^{-j2\omega t} \left\{ \langle v_a \rangle_1{}^* + \langle v_b \rangle_1{}^* e^{j2\pi/3} + \langle v_c \rangle_1{}^* e^{-j2\pi/3} \right\}. \end{aligned} \tag{83}$$

As seen in (83), the first term is DC which represents the positive sequence (DP index *k*=0); the second term is the second harmonic component which represents the negative sequence (DP index *k*=2). The final DP voltage vector is derived as

$$\begin{aligned} \vec{v}_{dq} = v_d + j v_q = \left\{ V_{d0} + j V_{q0} \right\} + e^{-j2\omega t} \left\{ V_{d2} + j V_{q2} \right\} \\ = \left\{ V_{d0} + V_{d2} \cos(2wt) + V_{q2} \sin(2wt) \right\} \\ + j \left\{ V_{q0} + V_{q2} \cos(2wt) - V_{d2} \sin(2wt) \right\}, \end{aligned} \tag{84}$$

where

$$V_{d0} = \frac{2}{3} Re \left\{ \langle v_a \rangle_1 + \langle v_b \rangle_1 e^{j2\pi/3} + \langle v_c \rangle_1 e^{-j2\pi/3} \right\}, \tag{85}$$

$$V_{q0} = \frac{2}{3} Im\{\langle v_a \rangle_1 + \langle v_b \rangle_1 e^{j2\pi/3} + \langle v_c \rangle_1 e^{-j2\pi/3}\},$$

$$V_{d2} = \frac{2}{3} Re\{\langle v_a \rangle_1{}^* + \langle v_b \rangle_1{}^* e^{j2\pi/3} + \langle v_c \rangle_1{}^* e^{-j2\pi/3}\},$$

$$V_{q2} = \frac{2}{3} Im\{\langle v_a \rangle_1{}^* + \langle v_b \rangle_1{}^* e^{j2\pi/3} + \langle v_c \rangle_1{}^* e^{-j2\pi/3}\}.$$

Since the *dq* components are in synchronous reference frame, both positive and negative sequence components $V_{dq,0}$ and $V_{dq,2}$ will become DC values in steady state, which makes it numerically efficient even for the unbalanced conditions.

The DP voltages for positive sequence $\langle v_{dq} \rangle_0$ and negative sequence $\langle v_{dq} \rangle_2$ in *dq* synchronous reference frame are expressed as

$$\begin{aligned} \langle v_d \rangle_0 &= V_{d0} \\ \langle v_q \rangle_0 &= V_{q0} \end{aligned} \tag{86}$$

$$\begin{aligned} \langle v_d \rangle_2 &= \frac{(V_{d2} - jV_{q2})}{2} \\ \langle v_q \rangle_2 &= \frac{(V_{q2} + jV_{d2})}{2}. \end{aligned} \tag{87}$$

The DP in *dq* synchronous reference frame can be transformed to *abc* stationary coordinates based on Park's transformation (8) using the DP convolution property as

$$\begin{bmatrix} \langle f_a \rangle_1 \\ \langle f_b \rangle_1 \\ \langle f_c \rangle_1 \end{bmatrix} = \langle T^{-1} \rangle_1 \begin{bmatrix} \langle f_d \rangle_0 \\ \langle f_q \rangle_0 \end{bmatrix} + \langle T^{-1} \rangle_1^* \begin{bmatrix} \langle f_d \rangle_2 \\ \langle f_q \rangle_2 \end{bmatrix}, \tag{88}$$

where T^{-1} is the inverse transformation matrix of T defined as

$$T^{-1} = \begin{bmatrix} \cos\omega t & -\sin\omega t \\ \cos(\omega t - 2\pi/3) & -\sin(\omega t - 2\pi/3) \\ \cos(\omega t + 2\pi/3) & -\sin(\omega t + 2\pi/3) \end{bmatrix}. \quad (89)$$

Since the DP index *k*=1 is considered for the *abc* coordinates only, the inverse transformation matrix (89) can be written in DP domain as

$$\langle T^{-1} \rangle_1 = \begin{bmatrix} \frac{1}{2} & j\frac{1}{2} \\ -\frac{1}{4} - j\frac{\sqrt{3}}{4} & -j\frac{1}{4} + \frac{\sqrt{3}}{4} \\ -\frac{1}{4} + j\frac{\sqrt{3}}{4} & -j\frac{1}{4} - \frac{\sqrt{3}}{4} \end{bmatrix} \quad (90)$$

3.6.2 DP Model Derivation

The DP model is derived from the time domain model. In this section, each component of DFIG in time domain is transformed to the DP domain using the properties (19), (20) and (21) [31][32]. In order for the DP model to be accurate and numerically efficient, the proper number of DP sets need to be selected. For the DFIG in *dq* synchronous reference frame, the positive and negative sequence DPs are selected as listed in the Table 3.1. The overall block diagram implementing the proposed DP model is shown in Figure 3.8. Based on the selected number of DP variables, the final model can be presented as follows:

DP Index	Component	Variables
k=0	Drive Train	T_m
k=0, 2	WRIG	$v_{dq,s}$, $v_{dq,r}$, $i_{dq,s}$, $i_{dq,r}$, $\psi_{dq,s}$, $\psi_{dq,r}$, ω_r, P_s, Q_s
	Controller	$x_{dq,1}$, $x_{dq,2}$, $i_{dqr,ref}$, $i_{dq,r}$, $\psi_{dq,s}$, $\psi_{dq,r}$

Table 3.1 Selected DP sets for the proposed model.

1) Wound Rotor Induction Generator (WRIG)

$$\frac{1}{\omega_b}\frac{d}{dt}\begin{bmatrix}\langle\psi_{ds}\rangle_k\\ \langle\psi_{qs}\rangle_k\end{bmatrix} = \begin{bmatrix}\langle v_{ds}\rangle_k\\ \langle v_{qs}\rangle_k\end{bmatrix} - R_s\begin{bmatrix}\langle i_{ds}\rangle_k\\ \langle i_{qs}\rangle_k\end{bmatrix} - \begin{bmatrix}0 & -1\\ 1 & 0\end{bmatrix}\begin{bmatrix}\langle\psi_{ds}\rangle_k\\ \langle\psi_{qs}\rangle_k\end{bmatrix} - j2\begin{bmatrix}\langle\psi_{ds}\rangle_k\\ \langle\psi_{qs}\rangle_k\end{bmatrix} \quad (91)$$

$$\frac{1}{\omega_b}\frac{d}{dt}\begin{bmatrix}\langle\psi_{dr}\rangle_k\\ \langle\psi_{qr}\rangle_k\end{bmatrix} = \begin{bmatrix}\langle v_{dr}\rangle_k\\ \langle v_{qr}\rangle_k\end{bmatrix} - R_s\begin{bmatrix}\langle i_{dr}\rangle_k\\ \langle i_{qr}\rangle_k\end{bmatrix} - \omega_{sl}\begin{bmatrix}0 & -1\\ 1 & 0\end{bmatrix}\begin{bmatrix}\langle\psi_{dr}\rangle_k\\ \langle\psi_{qr}\rangle_k\end{bmatrix} - j2\begin{bmatrix}\langle\psi_{dr}\rangle_k\\ \langle\psi_{qr}\rangle_k\end{bmatrix} \quad (92)$$

$$\begin{bmatrix}\langle\psi_{ds}\rangle_k\\ \langle\psi_{qs}\rangle_k\\ \langle\psi_{dr}\rangle_k\\ \langle\psi_{qr}\rangle_k\end{bmatrix} = \begin{bmatrix}X_s & 0 & X_m & 0\\ 0 & X_s & 0 & X_m\\ X_m & 0 & X_r & 0\\ 0 & X_m & 0 & X_r\end{bmatrix}\begin{bmatrix}\langle i_{ds}\rangle_k\\ \langle i_{qs}\rangle_k\\ \langle i_{dr}\rangle_k\\ \langle i_{qr}\rangle_k\end{bmatrix} \quad (93)$$

2) Mechanical System

$$\frac{d}{dt}\langle\omega_r\rangle_k = \frac{\langle T_e\rangle_k - \langle T_m\rangle_k}{2H} - jk\omega_s\langle\omega_r\rangle_k \quad (94)$$

3) RSC Controller

$$\begin{aligned}\frac{d}{dt}\langle x_d\rangle_k &= K_{I1}\left(\langle i_{dr,ref}\rangle_k - \langle i_{dr}\rangle_k\right) - jk\omega_s\langle x_d\rangle_k\\ \langle v_{dr}\rangle_k &= \langle x_{d2}\rangle_k + K_{P1}\left(\langle i_{dr,ref}\rangle_k - \langle i_{dr}\rangle_k\right)\\ \frac{d}{dt}\langle x_q\rangle_k &= K_{I2}\left(\langle i_{qr,ref}\rangle_k - \langle i_{qr}\rangle_k\right) - jk\omega_s\langle x_q\rangle_k\\ \langle v_{qr}\rangle_k &= \langle x_{q2}\rangle_k + K_{P2}\left(\langle i_{qr,ref}\rangle_k - \langle i_{qr}\rangle_k\right)\end{aligned} \quad (95)$$

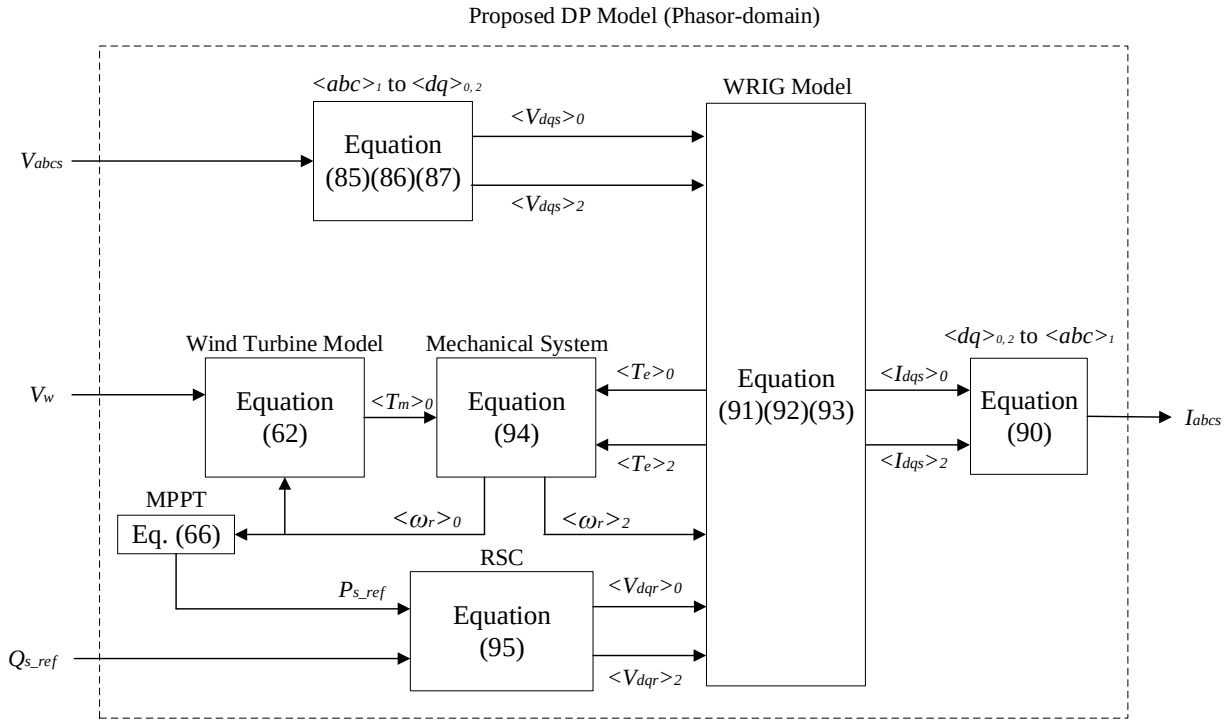

Figure 3.8 Overall block diagram of proposed DP model.

3.6.3 Reduced-order Dynamic Phasor Model (DP-ROM)

For the large-scale transient stability studies, neglecting stator electric transients is a common practice to enhance the simulation efficiency. The detail theory is well documented in [36] [49]. Based on this theory, it is straightforward to derive the reduced-order model by setting the term $\frac{d}{dt}\langle\psi_{dq,s}\rangle_k$ to zero. Therefore, the final DP-ROM model of WRIG is expressed as

$$0 = \begin{bmatrix}\langle v_{ds}\rangle_k \\ \langle v_{qs}\rangle_k\end{bmatrix} - R_s\begin{bmatrix}\langle i_{ds}\rangle_k \\ \langle i_{qs}\rangle_k\end{bmatrix} - \begin{bmatrix}0 & -1 \\ 1 & 0\end{bmatrix}\begin{bmatrix}\langle \psi_{ds}\rangle_k \\ \langle \psi_{qs}\rangle_k\end{bmatrix} - j2\begin{bmatrix}\langle \psi_{ds}\rangle_k \\ \langle \psi_{qs}\rangle_k\end{bmatrix} \tag{96}$$

$$\begin{aligned}&\frac{1}{\omega_b}\frac{d}{dt}\begin{bmatrix}\langle \psi_{dr}\rangle_k \\ \langle \psi_{qr}\rangle_k\end{bmatrix} \\ &= \begin{bmatrix}\langle v_{dr}\rangle_k \\ \langle v_{qr}\rangle_k\end{bmatrix} - R_s\begin{bmatrix}\langle i_{dr}\rangle_k \\ \langle i_{qr}\rangle_k\end{bmatrix} - \omega_{sl}\begin{bmatrix}0 & -1 \\ 1 & 0\end{bmatrix}\begin{bmatrix}\langle \psi_{dr}\rangle_k \\ \langle \psi_{qr}\rangle_k\end{bmatrix} - j2\begin{bmatrix}\langle \psi_{dr}\rangle_k \\ \langle \psi_{qr}\rangle_k\end{bmatrix}\end{aligned} \tag{97}$$

$$\begin{bmatrix} \langle \psi_{ds} \rangle_k \\ \langle \psi_{qs} \rangle_k \\ \langle \psi_{dr} \rangle_k \\ \langle \psi_{qr} \rangle_k \end{bmatrix} = \begin{bmatrix} X_s & 0 & X_m & 0 \\ 0 & X_s & 0 & X_m \\ X_m & 0 & X_r & 0 \\ 0 & X_m & 0 & X_r \end{bmatrix} \begin{bmatrix} \langle i_{ds} \rangle_k \\ \langle i_{qs} \rangle_k \\ \langle i_{dr} \rangle_k \\ \langle i_{qr} \rangle_k \end{bmatrix}. \quad (98)$$

Other than the WRIG model, all other components in Figure 3.8 are used for implementing the DP-ROM model. The DP-ROM model will be compared with the reference model in terms of accuracy and numerical efficiency in the next chapter.

3.7 Chapter Summary

In this chapter, each component of DFIG model has been derived for both EMT and DP model. Based on (91) – (95), for balanced condition, the DP and EMT model are equivalent. The negative sequence DP is activated for the unbalanced conditions, which enables the DP model to maintain the accuracy and numerical efficiency. In the next chapter, both EMT and DP model will be tested in SMIB network to measure the accuracy and numerical efficiency of the proposed model.

Chapter 4: Simulation Results Analysis of SMIB

In order to evaluate the accuracy and numerical efficiency of each model discussed in this thesis, both slow and fast transients are simulated in a single-machine infinite bus (SMIB) system. The DFIG and controller parameters are summarized in Table A.2 in Appendix A.2. For a fair comparison, the same *ode23t* (mod. Stiff / trapezoidal) solver in MATLAB/Simulink® [45] is used. The maximum step size is set to 1/60s, and absolute and relative tolerances are set to 10^{-3} and 10^{-4}, respectively. The implicit *ode23t* solver is selected since its size is not limited by the small time constants of the system due to numerical instability [50], but the automatic step size control algorithm dynamically adjust the step size to maximize the simulation efficiency while satisfying the error tolerance constraints [45].

Both accuracy and numerical efficiency are evaluated. For evaluation of numerical efficiency, the number of time steps taken by each model is recorded along with time step size. For evaluation of accuracy, the electromagnetic torque T_e of proposed DP & DP-ROM model are compared with the reference EMT model. Since the electromagnetic torque is a cross product of the flux and current, it can be used as a good reference for comparisons.

For the purpose of comparison with the reference time-domain solutions, the corresponding instantaneous value in DP-domain can be converted into time-domain based on (27) as

$$x(t) \cong Re\left\{\sum_{k\in K} X_k(t)\cdot e^{jk\omega_s t}\right\}. \tag{99}$$

For example, electromagnetic torque can be approximated as

$$T_e(t) \cong \langle T_e \rangle_0 + Re\{\langle T_e \rangle_2\} \cos(2\omega_s t) - Im\{\langle T_e \rangle_2\} \sin(2\omega_s t). \quad (100)$$

Two categories of computer studies are considered in this chapter: slow and fast transients. For the slow transient, the DFIG's starting transient and step change in references P_s and Q_s are simulated. For the fast transient, the grid side disturbances such as the three-phase balanced voltage dip (all phases are reduced by 50%) and unbalanced voltage dip (only one or two phases are reduced by 50%) are simulated.

4.1 Slow Transient Simulation

4.1.1 Start-up

The start-up of DFIG is simulated by setting the initial conditions of the models and their respective controllers to zero. A constant wind speed of 12m/s is applied, which corresponds to 0.73 pu of mechanical torque and 0.9 pu rotor speed in steady state. Since the inertia of WRIG is relatively large (H=5.5s), the machine reaches its steady state in approximately 20s. The computed transient responses produced by the considered models are compared in Figure 4.1 and Figure 4.2. As expected, the electromagnetic torque and rotor speed reach the desired operating point for both EMT and DP & DP-ROM Models. Since the starting transient is a balanced event, only the DP index *k*=0 is activated.

The qualitative analysis is applied for evaluating the accuracy by comparing the result of the simulations shown in Figure 4.1 and Figure 4.2. For the numerical efficiency, total number of

time steps taken by each model is recorded, and the average time step size is calculated and listed in Table 4.1.

As seen in Figure 4.1, there is a fundamental frequency oscillations that last from zero to approximately three seconds. The time step size during the first 3.5 seconds are depicted in Figure 4.3 for more intuitive comparison. Based on Figure 4.1 and Figure 4.3, it can be concluded that the numerical performance of DP model is better than that of the EMT model, as it uses a larger time step size. For the DP-ROM model, the time step size is at its maximum value 16.7 ms throughout the simulation and its trajectory is highly accurate with minor errors. Since the stator transients are neglected, there is no fundamental oscillation observed for the DP-ROM model.

According to Figure 4.3, DP model reaches to fairly large time step size after the transient is gone. Therefore, the majority part of the time steps taken for the DP model is the first 3s during the transient.

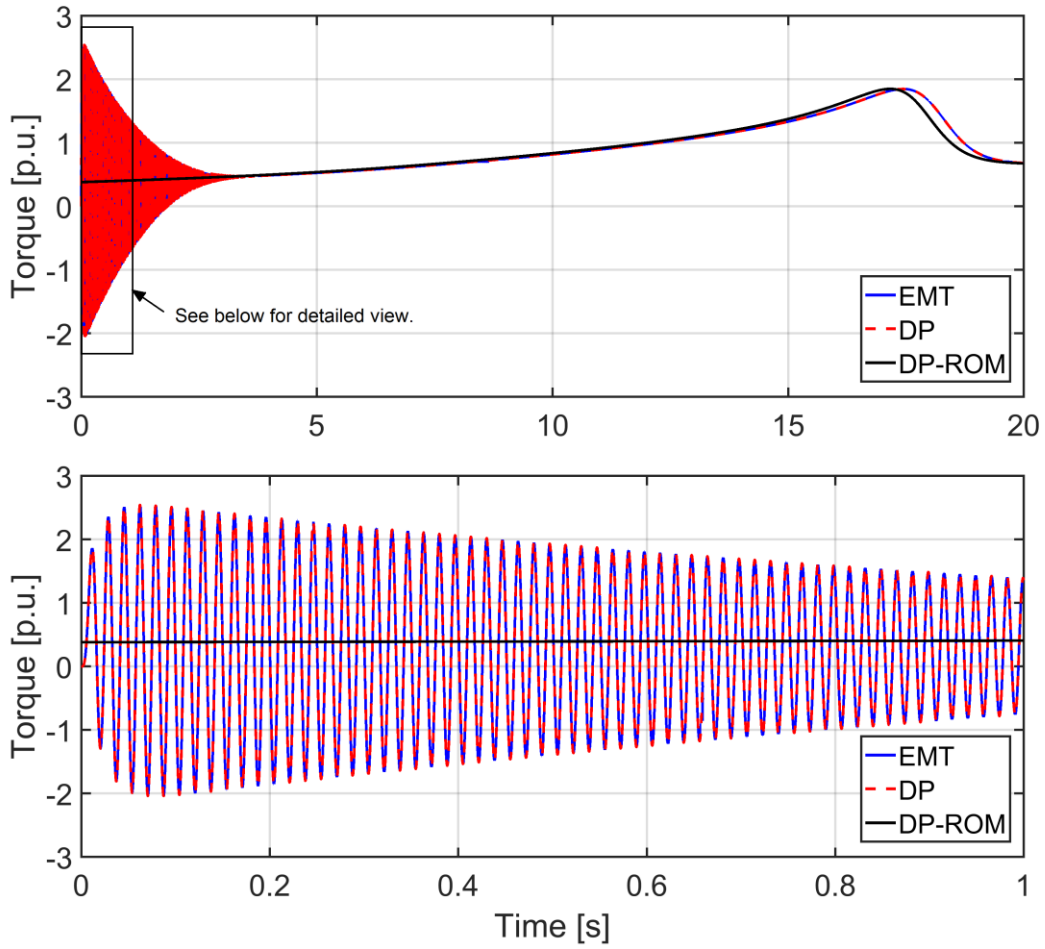

Figure 4.1 Start-up transient of DFIG comparison of torque T_e as predicted the considered models.

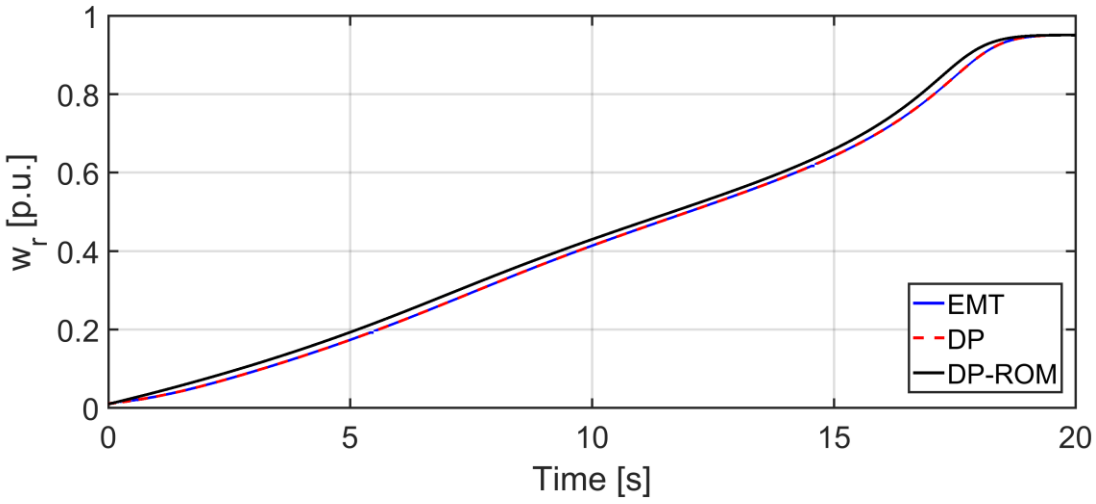

Figure 4.2 Start-up transient of DFIG comparison of speed ω_r as predicted the considered models.

Model	Simulation time: 20 s	
	Total Number of Time Steps	Average Time Step Size [ms]
EMT	66,692	0.30
DP	2,885	6.93
DP-ROM	1,205	16.7

Table 4.1 Total number of time steps taken for each model for starting transient.

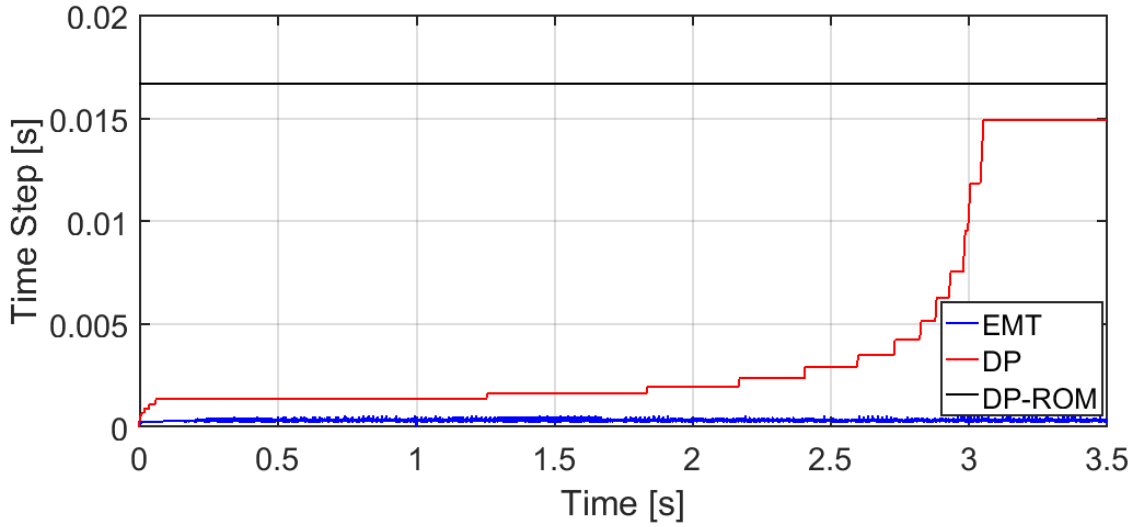

Figure 4.3 Comparison of time step size during the first 3.5s of the start-up transient study.

4.1.2 Response to Changes in References for P_s and Q_s

A step change in reference signals P_s and Q_s is analyzed to check the performance of decoupled control scheme. As explained in Section 3.4, the *d* and *q*-axis controls active and reactive powers, respectively, by controlling the current in each axes as shown in Figure 4.4

In the following study, the DFIG is assumed to be initialized and operating in a steady-state condition with mechanial torque T_m=0.73 pu. At t = 5 s, the active power reference is reduced by 50% while the reactive power reference remains constant. At t = 7 s, the active power reference is reduced by 50% while the reactive power reference remains constant. The results of this transient as predicted by the considered models are depicted in Figure 4.4. As expected, both *d* and *q*-axis rotor currents follow their reference signals correctly and the transient trajectories are the same since *d* and *q* axis control loop has the same PI controller parameters.

A response in electromagnetic torque is shown in Figure 4.5. The electromagnetic torque is first changed to a new steady state which is 50% of the original value. During the second change in the reactive power reserence, the torque oscillation quickly die out and it returns to the same value as shown in Figure 4.5.

In Figure 4.5, there is a slight mismatch for the results predicted by the DP-ROM model, which is due to simplifying assumptions used in this model. Regarding the numerical efficiency, both DP and DP-ROM models show superior performance in terms of the time step size during the changes in reference signals as shown in Figure 4.6.

In Figure 4.6, the time step size hits almost zero at t = 5 s and t = 7 s due to the sudden changes in reference signals; however, it takes only few time steps for both DP and DP-ROM model to reach the steady-state. Therefore, it can be concluded that the DP-ROM model is higly accurate during the slow transient conditions.

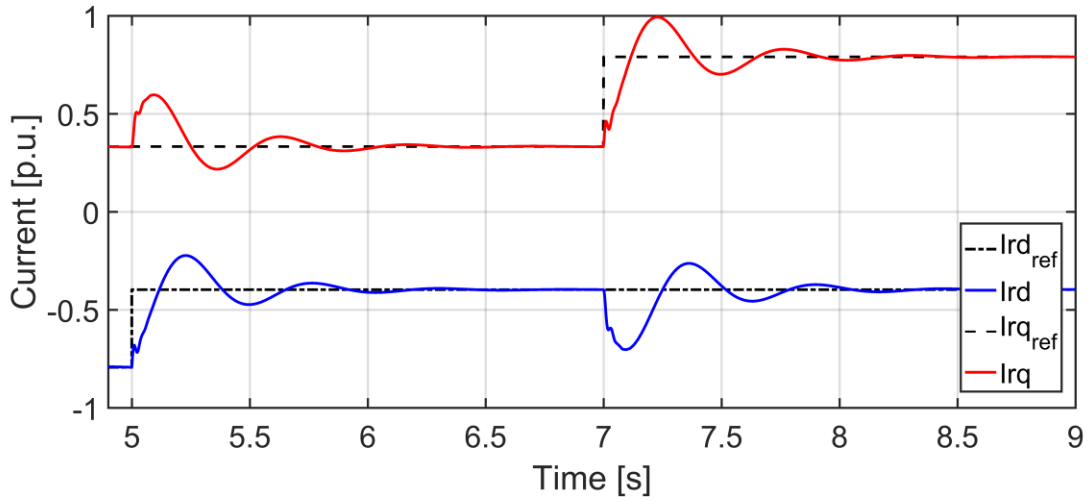

Figure 4.4 Response in currents i_{rd} and i_{rq} due to changes active and reactive power references.

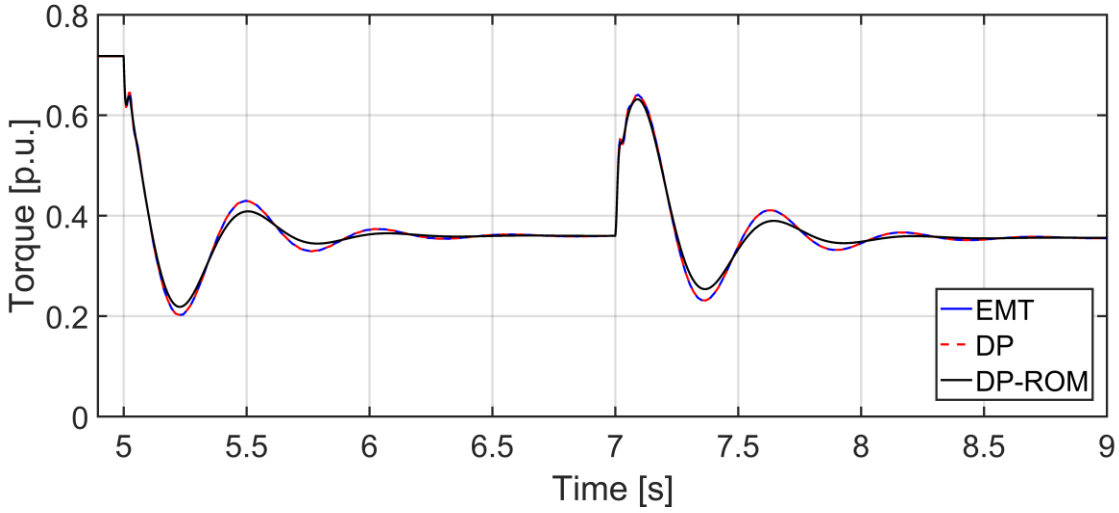

Figure 4.5 Response in torque T_e due to changes reference active and reactive power as predicted by the considered models.

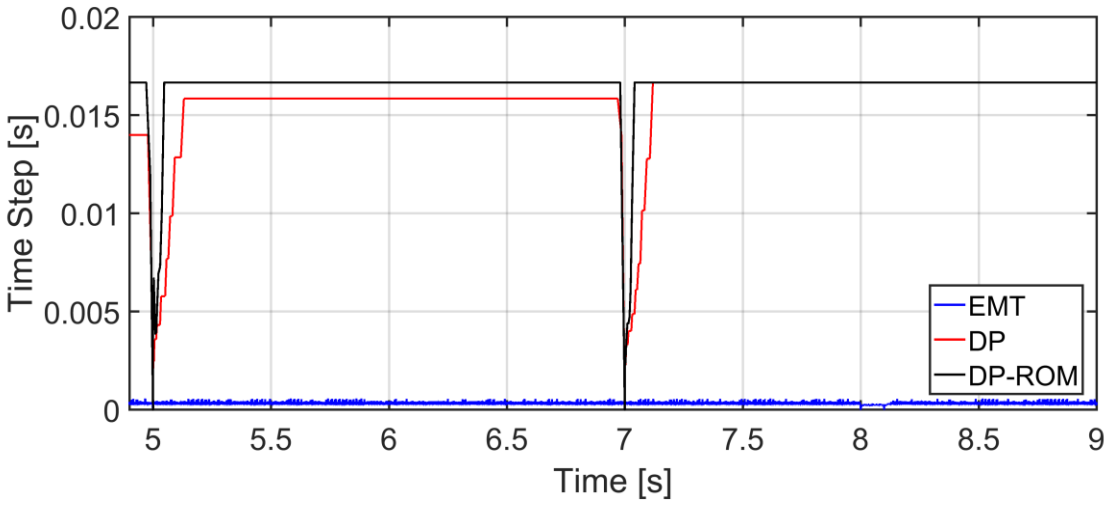

Figure 4.6 Time step size comparison for a step change of the controller reference signal.

4.2 Fast Transient Simulation

A short-term balanced and unbalanced voltage dip by 50% is considered for investigation of models' performance during fast transients. A fault is applied at t = 3s for 6 cycles (0.1s at 60 Hz). For consistency, the same numerical solver and same operating condition were used here as in the slow transient cases.

4.2.1 Balanced Disturbance

First, a balanced 50% voltage dip was applied to the grid side to all three phases at t = 3s. The fault is removed by restoring the voltages at t = 3.1s. The results of electromagnetic torque as predicted by the considered models are depicted in Figure 4.7. As it is a balanced disturbance, there is an oscillation of fundamental frequency without higher order harmonics after the disturbance is applied. Since only DP index k=0 is activated for DP and DP-ROM models, it is expected for both DP and EMT models to have the identical results, as can be seen in Figure 4.7.

To compare the numerical efficiency, total number of time steps taken by each model and the average time step size during the voltage dip and recovery period up to 5s are summarized in Table 4.2. Based on the information in Table 4.2 and Figure 4.8, it can be concluded that the proposed DP-ROM model is suitable for the large-scale power system stability studies as its time step size is large than 5ms during and after the fault.

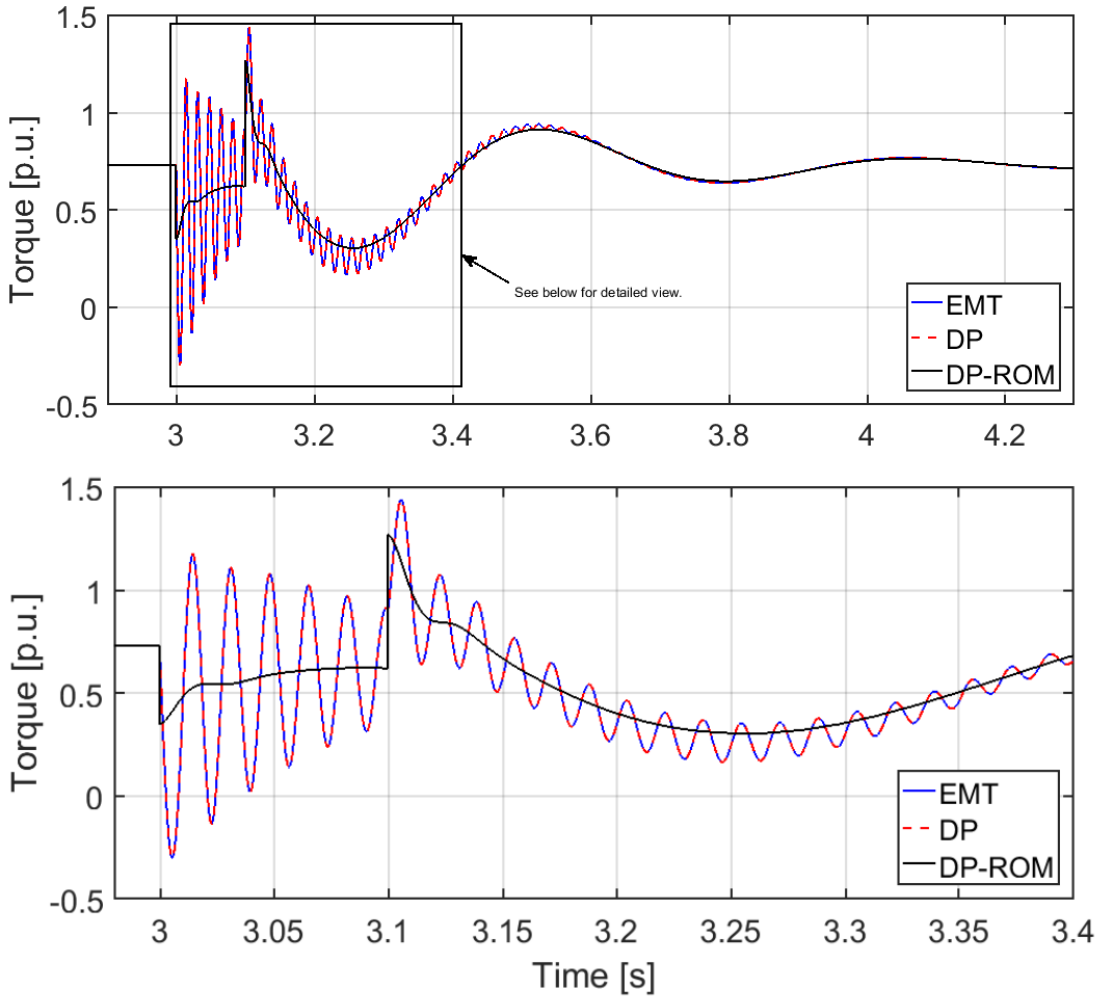

Figure 4.7 Transient in torque T_e due to short balanced 50% voltage dip as predicted by the considered models.

Model	Simulation time: 2.9 – 5 s	
	Total Number of Time Steps	Average Time Step [ms]
EMT	7,987	0.27
DP	507	4.17
DP – ROM	132	15.86

Table 4.2 Total number of time steps taken for each model for a balanced voltage dip (50%).

To show the numerical efficiency and how the step size was changing during the transient, the time step size variations from t = 2.9s to 4.3 s are depicted in Figure 4.8. Since there is an abrupt change in variables (e.g. in torque) due to the disturbance, the time step size hits almost zero at t = 3 s and 3.1s for all considered models. For the DP-ROM model, the step size is recovered to about 17 ms in one time step right after the sudden change. However, for the full DP model, the time steps slowly increase and recovers only after the fast oscillations completely die out after t = 4.2s, which is consistent with results of Figure 4.7.

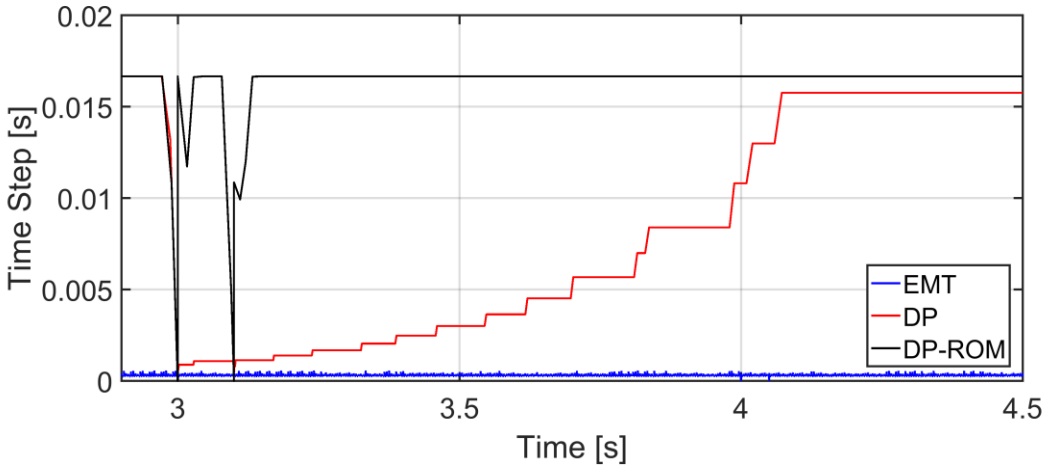

Figure 4.8 Comparison of time step size for 50% balanced voltage dip as taken by considered models.

4.2.2 Unbalanced Disturbance

In this section, a 50% unbalanced voltage dip in *a*-phase is applied at the grid side. The voltage is restored after 6 cycles, and the system goes through the fast transient. The results in calculated electromagnetic torque predicted by the considered models are shown in Figure 4.9.

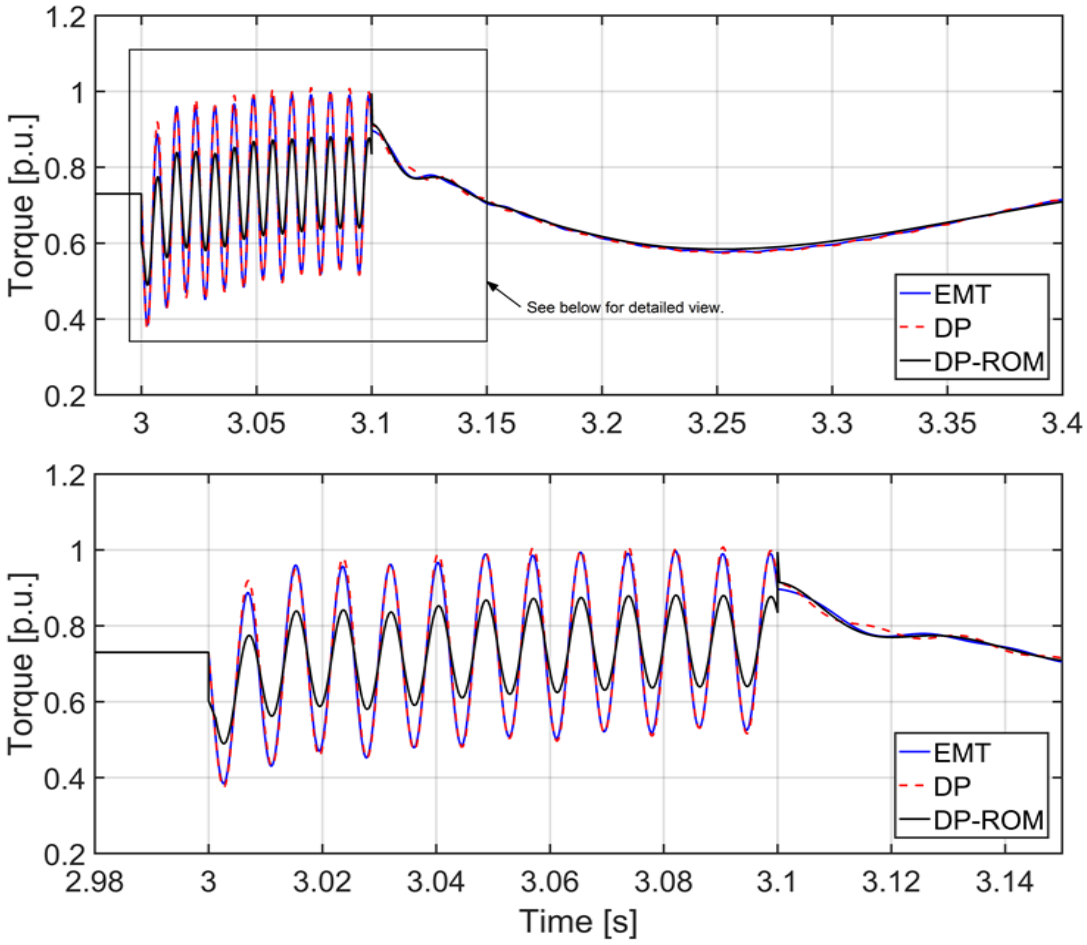

Figure 4.9 Comparison of torque T_e for unbalanced 50% voltage dip at *a*-phase as predicted by the considered models.

A noticeable change is that there is now a double frequency oscillation in the torque that is predicted by all models. This is due to the negative sequence present the during the unbalanced voltage dip. Therefore, the DP index k=0 and k=2 are activated for both DP and DP-ROM models. As expected, the trajectory of DP-ROM model traverse the average value of the reference model with fairly large time step size. Also, there is a mismatch between the DP and EMT models during and after the voltage dip, which is less than 2%. For comparison of numerical efficiency, the total number of time steps and the average time step size as taken by the considered models are summarized in Table 4.3.

Model	Simulation time: 2.9 – 5 s	
	Total Number of Time Steps	Average Time Step [ms]
EMT	8,129	0.26
DP	611	3.44
DP – ROM	142	14.70

Table 4.3 Total number of time steps taken for each model for an unbalanced voltage dip (50%).

Compared to the balanced disturbance case, the average time step size is slightly reduced. For the DP-ROM model, it is still suitable for typical transient stability programs since the time step generally remains well above 5 ms (except for the voltage' sudden changes at t = 3s and 3.1s, respectively).

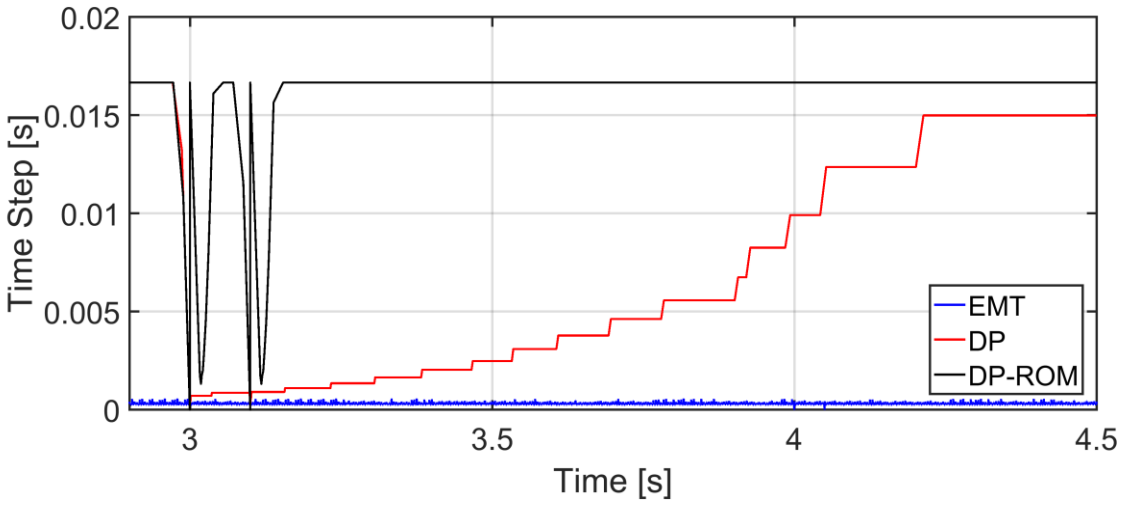

Figure 4.10 Comparison of time step size for 50% unbalanced voltage dip at *a*-phase as taken by considered models.

4.3 Chapter Summary

In this chapter, the slow and fast transient cases were investigated using a SMIB system to verify the accuracy and numerical efficiency of the proposed DP model by comparing the trajectory of electromagnetic torque and the total number of time steps with time step size with alternative models. The total number of time steps and the average time step size are compared to measure the numerical efficiency of each model. Based on the studies with SMIB system, the proposed DP and DP-ROM model is validated and is shown to have advantages in terms of accuracy and numerical efficiency.

Chapter 5: Simulation Result Analysis of Two-area Four-machine Network

In this test case, both balanced and unbalanced disturbances are applied to the point of interconnection (POI) of the WPP to assess the benefit of using the proposed model. The WPP is represent by an aggregated DP-ROM model. The interconnected WPP is rated as 6 MW WPP and aggregated as a single equivalent machine representing four identical 1.5 MW DFIGs, which is a reasonable assumption according to literature [19].

5.1 Description of Simulation Setup

In order to test the proposed DP approach for transient stability study, the DP-ROM model is interconnected to the two-area four-machine network depicted in Figure 5.1,which is a built-in model in Simscape^{TM} Power Systems^{TM} [51] in MATLAB/Simulink program. The purpose of transient stability study is to analyze the slower electromechanical transients [36]. Therefore, the DP-ROM model is connected to bus 10, which is the point of interconnection (POI) for this test case.

The two-area four-machine network of Figure 5.1 consists of four sets of synchronous generators with dedicated governor, excitation system, and power system stabilizers (two sets per each area). The generators are interconnected through transformers and transmission lines. The system parameters are summarized in the Appendix A.3, and a brief description of components is provided below:

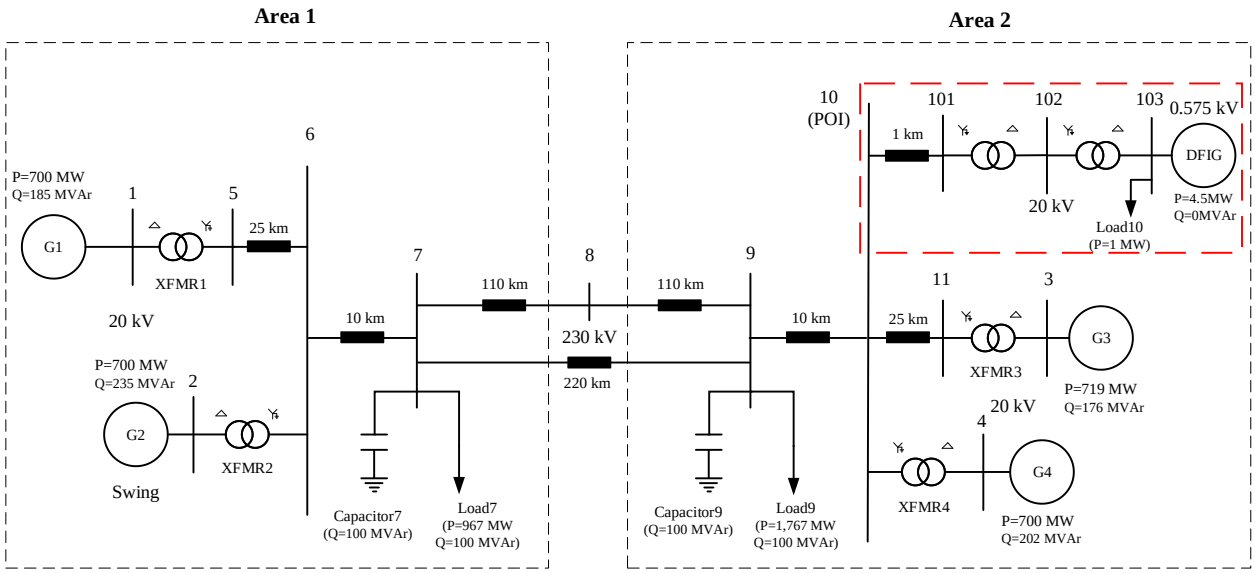

Figure 5.1 Single line diagram of two-area four-machine network with interconnected WPP.

1) Overview of the network model

Unlike other transient stability software such as PSS/E[52], the test case network has the following distinctive feature;

- Three-phase phasor domain is considered instead of positive sequence single-phase network. In this way, the actual response of positive sequence and negative sequence can be obtained to test the proposed dynamic phasor model.

2) Synchronous generator model

The four synchronous generators are modeled using a sixth-order state-space model described in Appendix B.1

3) **Steam turbine and governor model**

A complete tandem-compound single mass steam prime mover, including a speed governing system is considered [53].

4) **Excitation model**

IEEE type 1 excitation model is implemented according to IEEE Standard 421.5-1992 without saturation function [54].

5) **Transmission line**

All transmission lines in the test case are modeled as three-phase ∏ section. The section consists of one set of series *RL* elements between input and output terminals and two sets of shunt capacitances lumped at both ends.

6) **Power System Stabilizer**

The conventional Delta w PSS from [36] is implemented.

5.2 Interconnection of Wind Farm

Before connecting the 6 MW WPP into the network at bus 10, in steady state the network is sending 413.9 MW active power from Area 1 to Area 2. After the WPP is interconnected to the Area 2 bus 10, it is expected for the network power flow to undergo some transient and after some time reach a new balanced steady state. The result of simulated interconnection transient as observed in real and reactive power flow between the two areas is shown Figure 5.2 and Figure 5.3, respectively. The WPP is initialized at the same operating point as defined in Chapter 4,

which is 0.73 pu of P_m and connected at t = 1s. Since the total power output at the terminal of WPP is 4.38 MW and 1MW load is connected at the bus 103, the total injected into the network is 3.38 MW. It is expected that change of reactive power flow is not significant as the WPP is operated in unity power factor.

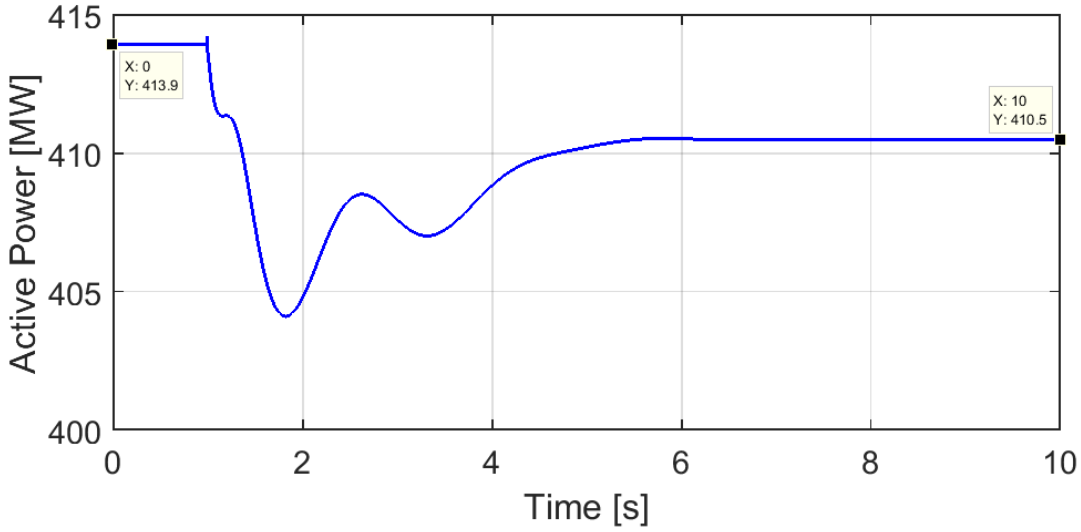

Figure 5.2 Transient observed in active power flow between the two areas due to interconnection of the wind farm.

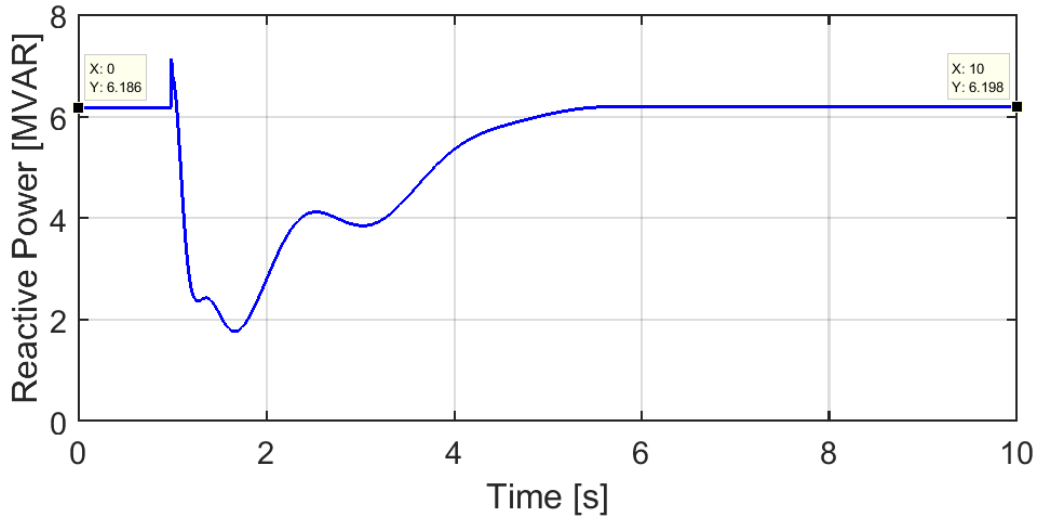

Figure 5.3 Transient observed in reactive power flow between the two areas due to interconnection of the wind farm.

5.3 Simulation of Fast Transient

In this section, the balanced and unbalanced faults are applied to the POI bus 10 to test the proposed DP-ROM model. Since the network reaches its new steady state in approximately 8 seconds, as shown in Figure 5.2 and Figure 5.3, the fault is applied at t = 8s for 6 cycles (0.1 second in 60 Hz). The fault impedance and ground impedance are set to 0.002 Ω and the same numerical solver and error tolerances are applied as described in Chapter 4.

5.3.1 Balanced Fault

The magnitude of POI voltage level is depicted in the Figure 5.4. The WPP's torque trajectory is depicted in Figure 5.5. Since the fault was cleared without any loss of equipment or lines in the network, the active power, reactive power, voltage, and electromagnetic torque level come back to their original steady state values as shown in Figure 5.4 and Figure 5.5. As shown in Figure 5.5, the torque becomes negative at t = 8s, which means that the WRIG operates as a motor during the fault. Once the fault is cleared and POI voltage level is recovered, the electromagnetic torque becomes positive and comes back to the original steady state after approximately 5 seconds.

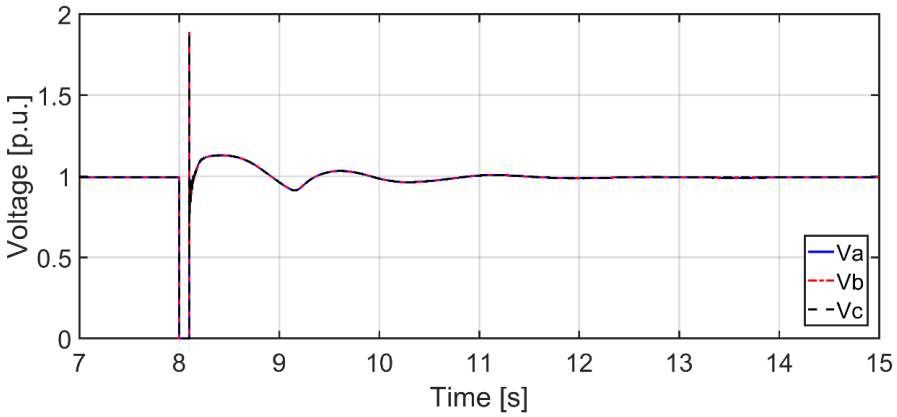

Figure 5.4 Voltage magnitude at the terminal of WPP for a balanced fault.

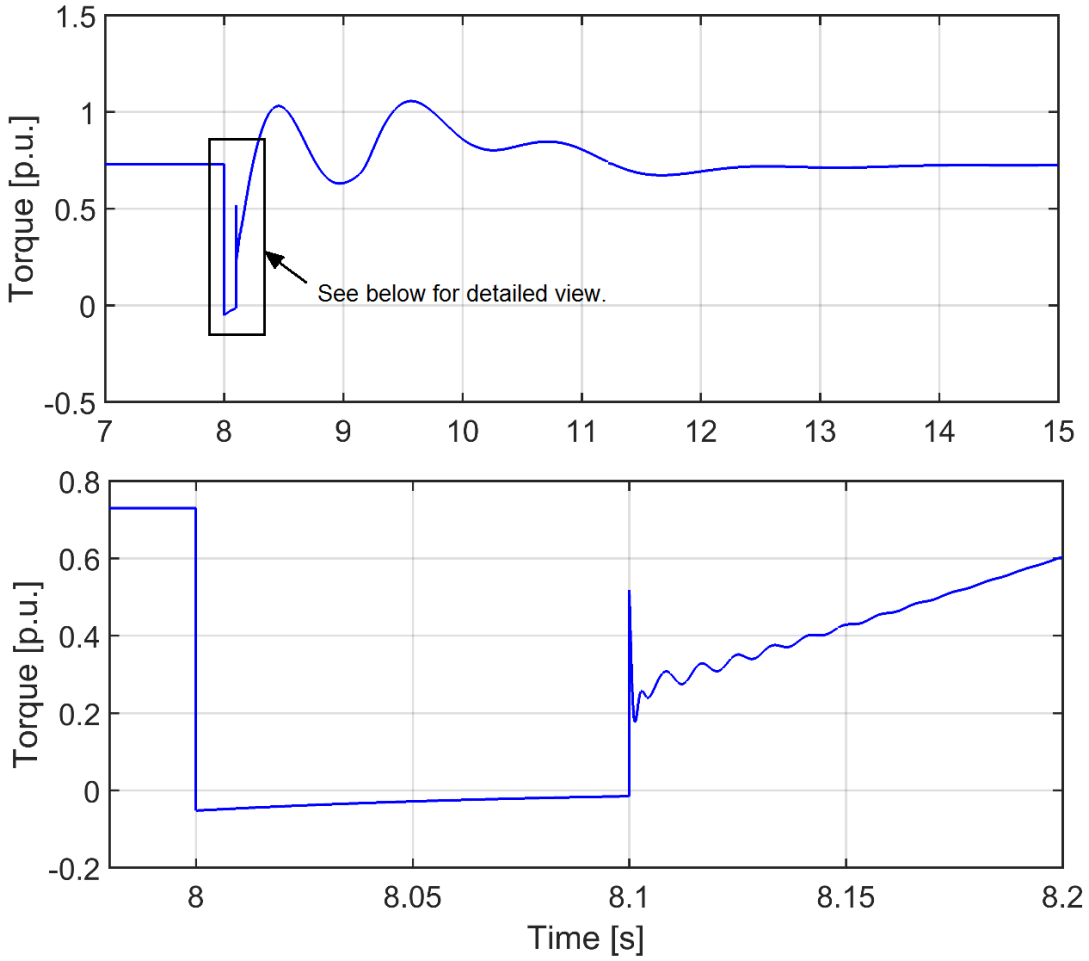

Figure 5.5 Torque T_e of the WPP during a balanced fault.

To verify the results of this study with the full-order DP model, the terminal voltage at the WPP shown in Figure 5.6 has been saved and injected into the EMT and DP models, as in the SMIB test case. Since it is a balanced disturbance, only the *a*-phase current of each model is depicted in Figure 5.7. As expected, the *a*-phase current trajectory of EMT and DP models match perfectly without any visible errors. Therefore, it can be concluded that the proposed DP model can be interconnected to the actual power networks and the results are expected to be highly accurate.

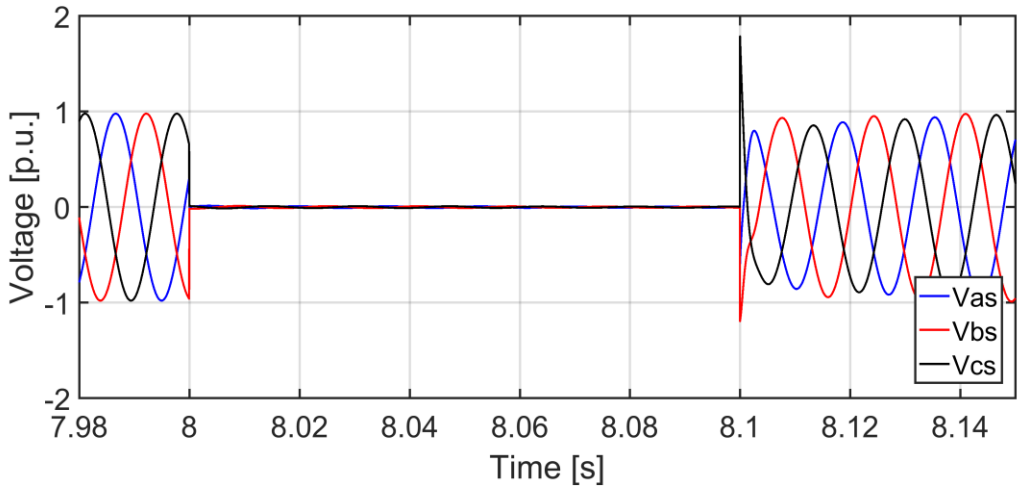

Figure 5.6 Recorded terminal voltage from the two-area four-machine network for a balanced fault.

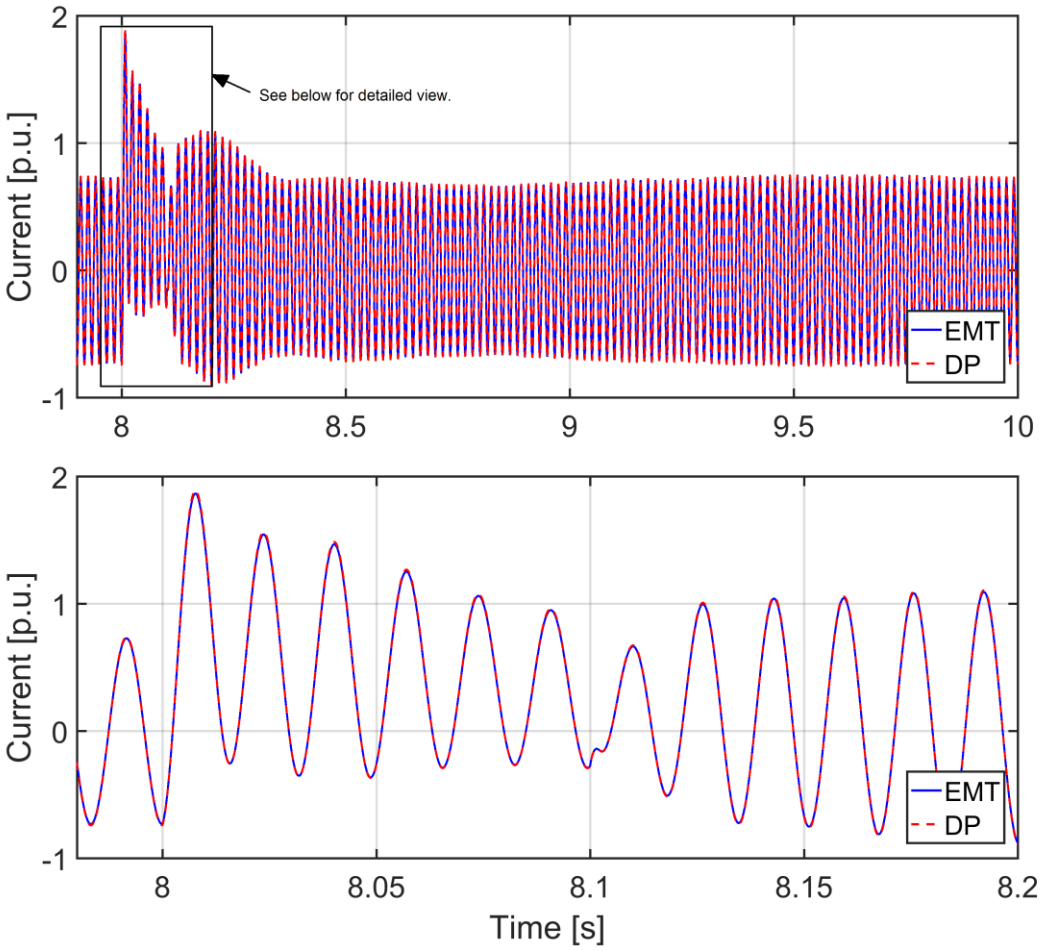

Figure 5.7 Result comparison of *a*-phase current for a balanced fault.

5.3.2 Unbalanced Fault

In this section, an unbalanced *a*-phase-to-ground fault is applied to the POI bus 10. The fault is cleared after 6 cycles. The magnitude of each phase voltage at the POI are depicted in the Figure 5.8. This unbalance voltage will activate the negative sequence DP. As depicted in Figure 5.9, there is a double frequency oscillation in electromagnetic torque during and after the fault. This phenomenon is well captured by the negative sequence network in the model and WPP.

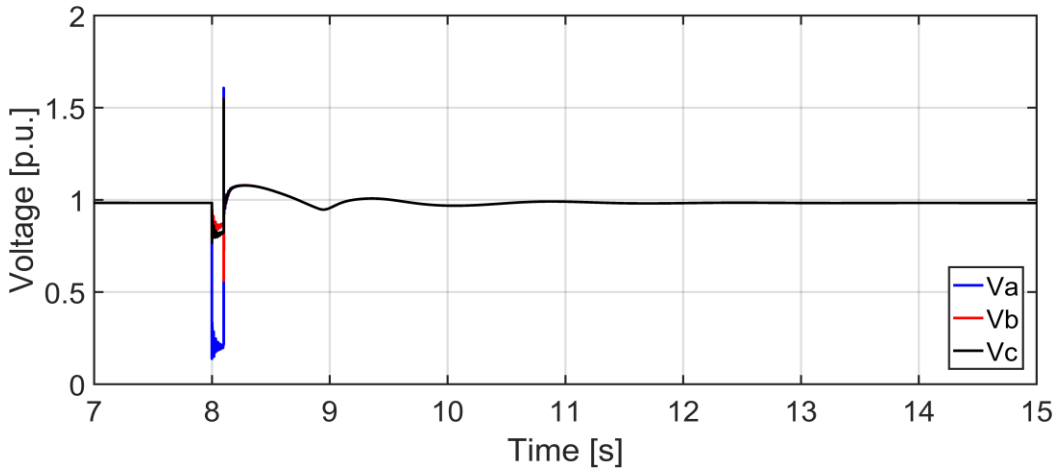

Figure 5.8 Voltage magnitude at the terminal of WPP for an unbalanced fault.

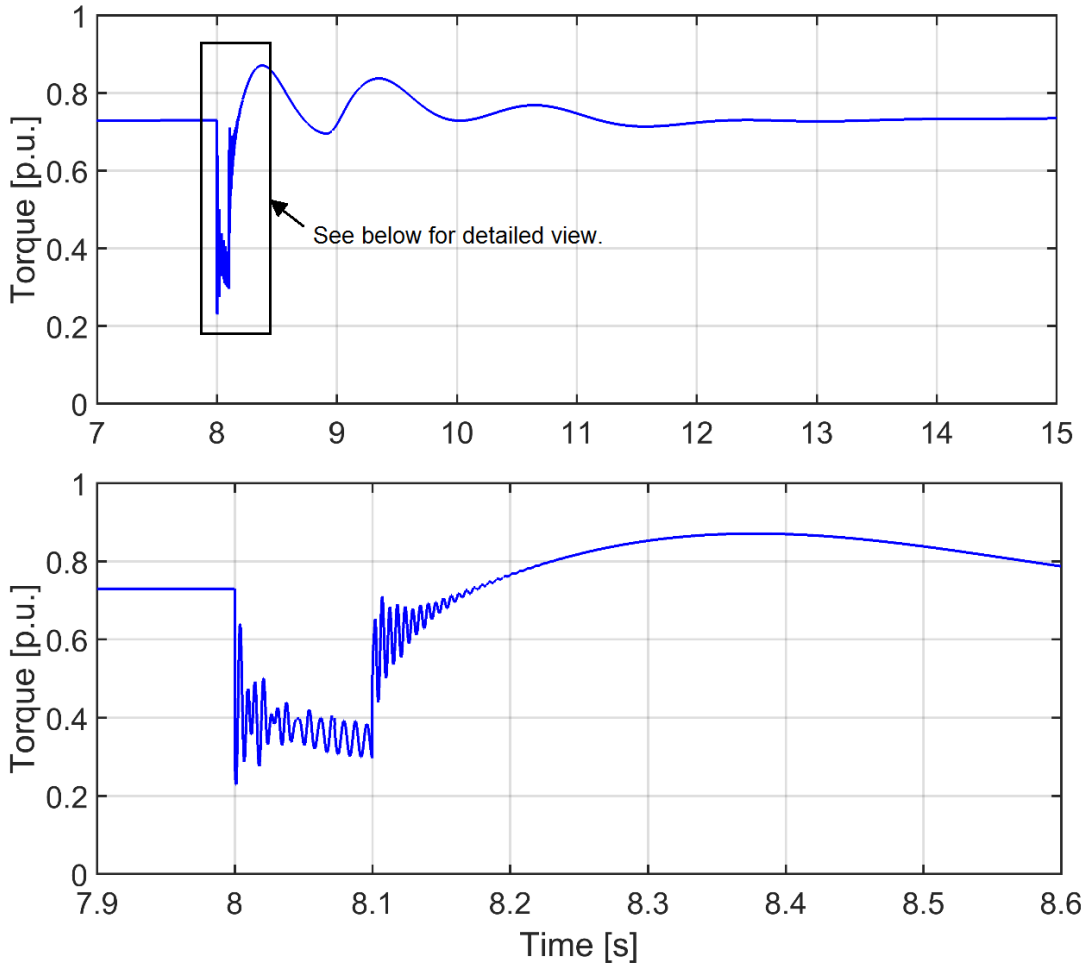

Figure 5.9 Te of the WPP for an unbalanced fault.

Since it is an unbalanced disturbance, the output current of WPP injected to the grid is the summation of positive sequence and negative sequence currents. For the purpose of model verification, the magnitude of both positive and negative sequence currents is compared in Figure 5.10.

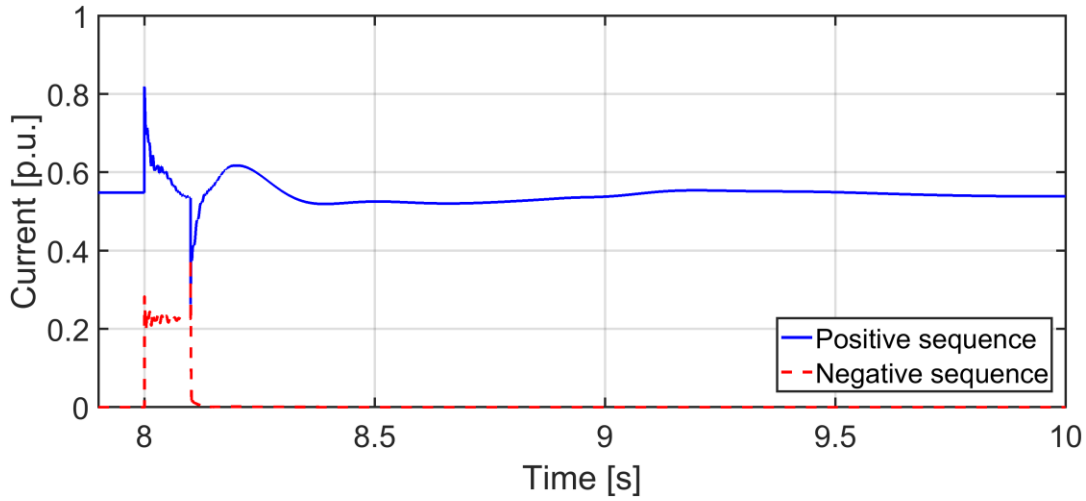

Figure 5.10 Magnitude of positive and negative sequence currents at the WPP during the unbalance fault.

As shown in Figure 5.10, the proposed DP model reacts to the grid side disturbance as expected. For more detail comparison and verification, the terminal voltage at the WPP has been saved and fed back into the EMT reference model. The reconstructed voltages in time-domain in *abc*-coordinates is depicted in Figure 5.11, and the faulty *a*-phase current is shown in Figure 5.12.

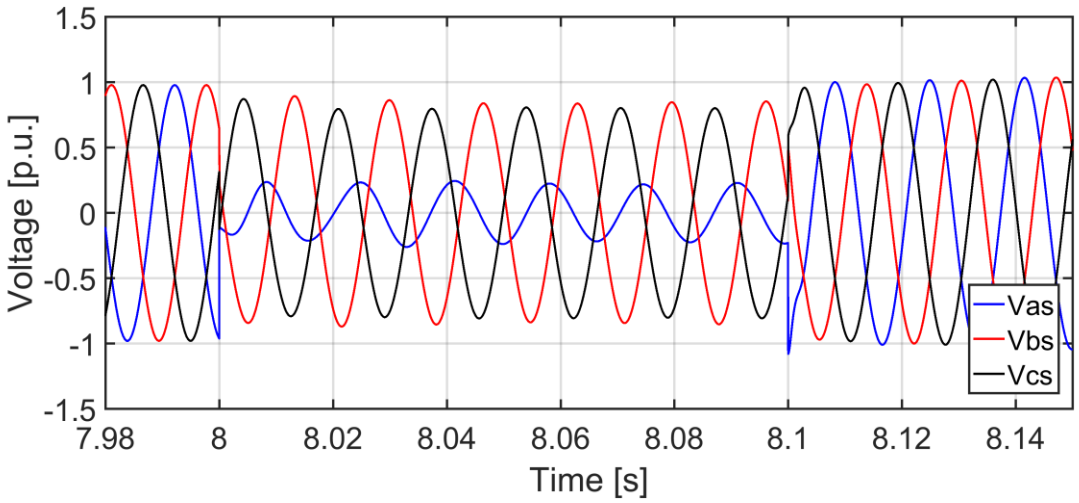

Figure 5.11 Terminal voltage at the WPP during an unbalanced fault.

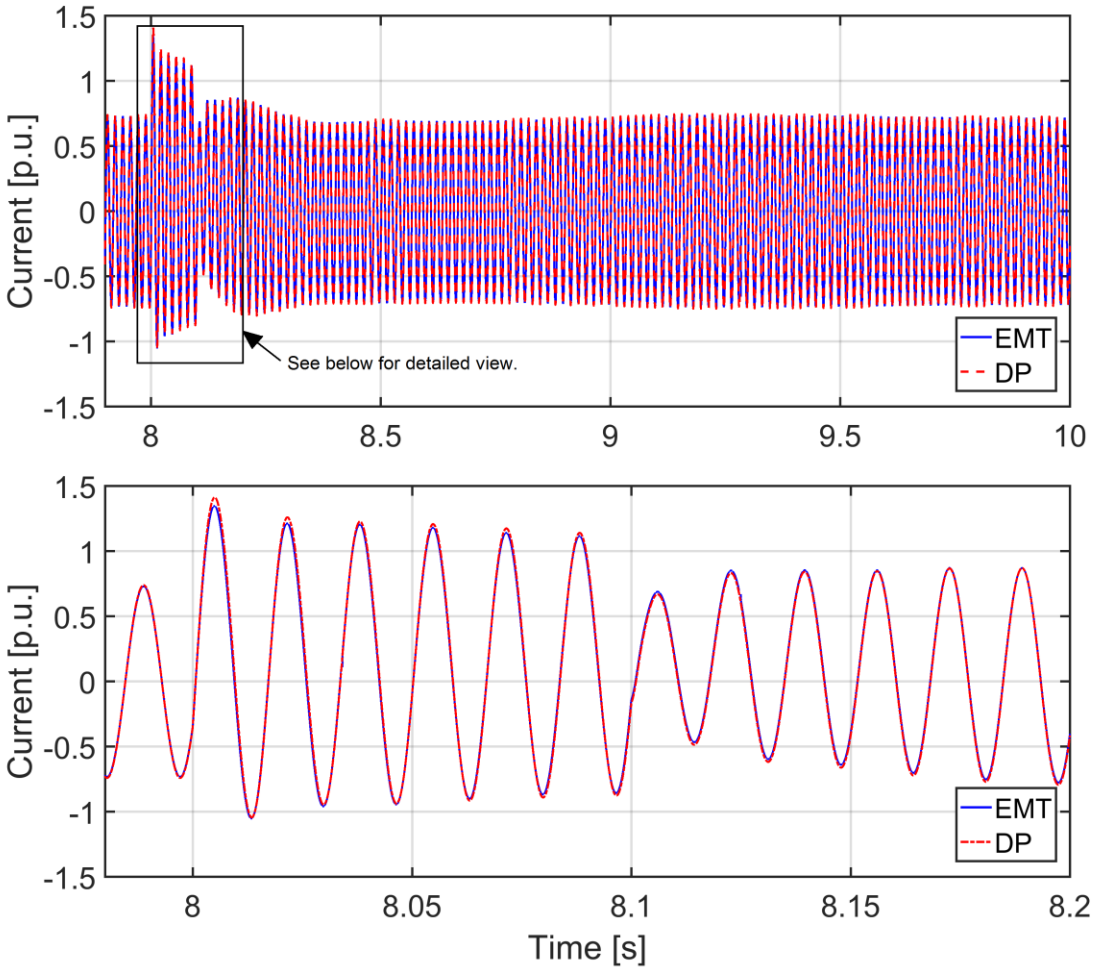

Figure 5.12 Comparison of *a*-phase current for an unbalanced fault as predicted by EMT and DP models.

As seen in Figure 5.12, there is a minor mismatch between two results. However, the mismatch is less than 2% and is consistent with what has been observed in Chapter 4. Therefore, it can be concluded that the proposed PD model works for unbalanced cases with a negligible error.

5.4 Chapter Summary

In this chapter, the balanced and unbalanced fault cases were tested using a two-area four-machine network to verify the proposed DP-ROM model and to demonstrate that it works for the power networks with other machines. For the verification purpose, the terminal voltage at the WPP was recorded and injected into the reference EMT model to check if the results are consistent and accurate with respect to the reference model. The result of this investigation was successful as the developed DP model represents both balanced and unbalanced fault cases well. Based on the test case in the two-area four-machine network case, the proposed DP and DP-ROM models have been validated in the power network where other machines are involved.

Chapter 6: Conclusion

6.1 Summary

The objective of the thesis is to derive the DP model of the commonly used DFIGs that can accurately capture both balanced and unbalanced conditions and is suitable for large scale transient stability studies. This is accomplished by dynamic phasor approach which can approximate the reference time-domain model using the selected sets of dynamic phasors. For the computational efficiency, positive and negative sequence DP sets have been selected in this thesis. Following steps are taken to derive and validate the proposed DP model.

1) Develop a reference model in time-domain.
2) Convert the reference model into dynamic phasor-domain.
3) Once the DP model is derived, the reduced-order model (DP-ROM) can be also developed by neglecting the stator dynamics. This DP-ROM is suitable for large scale transient stability analysis.
4) Both DP and DP-ROM models are tested using SMIB network. The transient responses are compared with the time domain reference model in terms of accuracy and numerical efficiency.
    a. Accuracy (Qualitative analysis): Comparing the result of predicted torque of the proposed model with the reference model the accuracy has been confirmed.
    b. Numerical efficiency (Quantities analysis): Based on the observed time step sizes, it was determined that the proposed DP model is accurate and computationally efficient even with fairly large time steps, comparable to those used in traditional TS programs.

5) Finally, the validated DP-ROM model is interconnected with two-area four-machine network to test the model performance more complicated scenarios with presence of other machines and components.

6.2 Significance and Contribution

The main contributions of this thesis are: An efficient model of DFIG in dynamic phasor domain has been provided for the large scale transient stability analysis. The model can include both positive and negative sequences, and may be reduced or full-order depending on excluding of including the stator transients. The accuracy of the developed PD model can approach that of EMT model. Using this approach, the other components of power network can be converted to the dynamic phasor domain so that the negative sequence network can be analyzed separately for more accurate simulations. This has a potential of significantly extending the range of application of TS programs with such DP models.

6.3 Future Research Directions

Since the aim of the thesis has been to derive the dynamic phasor model of DFIG for transient stability studies, there are many possible research directions related to the modeling of power systems based on the dynamic phasor approach. The following could be possible research directions for further investigation in terms of large scale power system studies.

1) Including the protection schemes that are used for LVRT requirement into the modelling. Since this thesis is mainly focused on machine and controller dynamics, the protective equipment dynamics are neglected. Therefore, it would be more practical for the wind

power plant interconnection studies to include the proper protection schemes into the DP models as well.

2) Derive DP-based models for other machines such as synchronous generators and inverter-based generators and test them in the same network. In this way, all generator units in the network will have dedicate positive and negative sequence network in phasor domain. It would be beneficial when analyzing unbalanced conditions in the network. The final result can be compared to the result of the typical transient stability analysis programs.

3) Extend the concept to analyze the sub-synchronous and super-synchronous resonance studies for a gird with series compensated transmission lines or potential torsional interactions between the wind turbine generator and the gird. One of the advantages of using the dynamic phasor approach is that other harmonic components can be easily added by selecting appropriate number of DP indexes.

Bibliography

[1] T. Mai *et al.*, "Renewable electricity futures for the United States," *IEEE Trans. Sustain. Energy*, vol. 5, no. 2, pp. 372–378, 2014.

[2] D. Kosterev and D. Davies, "System model validation studies in WECC," *IEEE PES Gen. Meet.*, pp. 1–4, 2010.

[3] J. C. Bailar, "Science, statistics, and deception," *Ann. Intern. Med.*, vol. 104, no. 2, pp. 259–260, 1986.

[4] B. Wu, Y. Lang, N. Zargari, and S. Kouro, *Power Conversion and Control of Wind Energy Systems*. IEEE Press, 2011.

[5] M. Behnke *et al.*, "Development and Validation of WECC Variable Speed Wind Turbine Dynamic Models for Grid Integration Studies," *AWEA's 2007 Wind. Conf.*, 2007.

[6] R. Pena, J. C. Clare, and G. M. Asher, "Doubly fed induction generator using back-to-back PWM converters and its application to variable-speed wind-energy generation," *IEE Proc. - Electr. Power Appl.*, vol. 143, no. 3, p. 231, 1996.

[7] I. Erlich, H. Wrede, and C. Feltes, "Dynamic behavior of DFIG-based wind turbines during grid faults," *2007 Power Convers. Conf. - Nagoya*, pp. 1195–1200, 2007.

[8] Z. Miao and L. Fan, "The art of modeling and simulation of induction generator in wind generation applications using high-order model," *Simul. Model. Pract. Theory*, vol. 16, no. 9, pp. 1239–1253, 2008.

[9] I. Erlich, J. Kretschmann, S. Mueller-Engelhardt, F. Koch, and J. Fortmann, "Modeling of wind turbines based on doubly-fed induction generators for power system stability studies," *IEEE Trans. Power Syst.*, vol. 22, no. 3, pp. 909–919, 2007.

[10] D. Kim, Y. Moon, and H. Nam, “A New Simplified Doubly Fed Induction Generator Model for Transient Stability Studies,” *IEEE Trans. Energy Convers.*, vol. 30, no. 3, pp. 1030–1042, 2015.

[11] M. A. SNYDER, “Development of Simplified Models of Doubly-Fed Induction Generators,” Ph.D. Dissertation, Chalmers University of Technology, 2012.

[12] N. W. Miller, J. J. Sanchez-Gasca, W. W. Price, and R. W. Delmerico, “Dynamic modeling of GE 1.5 and 3.6 MW wind turbine-generators for stability simulations,” *2003 IEEE Power Eng. Soc. Gen. Meet. (IEEE Cat. No.03CH37491)*, vol. 3, pp. 1977–1983, 2003.

[13] P. Pourbeik *et al.*, “Generic stability models for type 3 & 4 wind turbine generators for WECC,” *2013 IEEE Power Energy Soc. Gen. Meet.*, pp. 1–5, 2013.

[14] E. Muljadi, Y. C. Zhang, V. Gevorgian, and D. Kosterev, “Understanding dynamic model validation of a wind turbine generator and a wind power plant,” *2016 IEEE Energy Convers. Congr. Expo.*, pp. 1–5, 2016.

[15] M. Asmine *et al.*, “Model Validation for Wind Turbine Generator Models,” *IEEE Trans. Power Syst.*, vol. 26, no. 3, pp. 1769–1782, 2011.

[16] D. Ochoa and S. Martinez, “A Simplified Electro-Mechanical Model of a DFIG-based Wind Turbine for Primary Frequency Control Studies,” *IEEE Lat. Am. Trans.*, vol. 14, no. 8, pp. 3614–3620, 2016.

[17] A. Honrubia-Escribano, E. Gómez-Lázaro, A. Vigueras-Rodríguez, A. Molina-Garcia, J. A. Fuentes, and E. Muljadi, “Assessment of DFIG simplified model parameters using field test data,” *2012 IEEE Power Electron. Mach. Wind Appl.*, pp. 1–7, 2012.

[18] J. Fortmann, S. Engelhardt, J. Kretschmann, C. Feltes, and I. Erlich, “New Generic Model

of DFG-Based Wind Turbines for RMS-Type Simulation," *IEEE Trans. Energy Convers.*, vol. 29, no. 1, pp. 110–118, 2014.

[19] A. Ellis, E. Muljadi, J. Sanchez-Gasca, and Y. Kazachkov, "Generic models for simulation of wind power plants in bulk system planning studies," *IEEE Power Energy Soc. Gen. Meet.*, pp. 1–8, 2011.

[20] S. R. Sanders, J. M. Noworolski, X. Z. Liu, and G. C. Verghese, "Generalized Averaging Method for Power Conversion Circuits," *IEEE Trans. Power Electron.*, vol. 6, no. 2, pp. 251–259, 1991.

[21] A. M. Stanković, S. R. Sanders, and T. Aydin, "Dynamic phasors in modeling and analysis of unbalanced polyphase AC machines," *IEEE Trans. Energy Convers.*, vol. 17, no. 1, pp. 107–113, 2002.

[22] T. Yang, "Development of Dynamic Phasors for the Modelling of Aircraft Electrical Power Systems," Ph.D Dissertation, The University of Nottingham, 2013.

[23] S. Henschel, "Analysis of Electromagnetic and Electromechanical Power System Transients with Dynamic Phasors," Ph.D. Dissertation, The University of British Columbia, 1999.

[24] Y. Levron and J. Belikov, "Modeling power networks using dynamic phasors in the dq0 reference frame," *Electr. Power Syst. Res.*, vol. 144, pp. 233–242, 2017.

[25] M. C. Chudasama and A. M. Kulkarni, "Dynamic phasor analysis of SSR mitigation schemes based on passive phase imbalance," *IEEE Trans. Power Syst.*, vol. 26, no. 3, pp. 1668–1676, 2011.

[26] T. Demiray, "Simulation of Power Systems Dynamics using Dynamic Phasor Models," *X Symp. Spec. Electr. Oper. Expans. Plan.*, pp. 0–9, 2006.

[27] P. K. Dash, K. K.r., and R. K. Patnaik, “Dynamic phasor and frequency estimation of time-varying power system signals,” *Int. J. Electr. Power Energy Syst.*, vol. 44, no. 1, pp. 971–980, 2013.

[28] G. Asher, S. Bozhko, and T. Yang, “Active front-end rectifier modelling using dynamic phasors for more-electric aircraft applications,” *IET Electr. Syst. Transp.*, vol. 5, no. 2, pp. 77–87, 2015.

[29] A. Coronado-Mendoza, J. L. Bernal-Agustín, and J. A. Domínguez-Navarro, “Photovoltaic boost converter system with dynamic phasors modelling,” *Electr. Power Syst. Res.*, vol. 81, no. 9, pp. 1840–1848, 2011.

[30] C. Liu, A. Bose, and P. Tian, “Modeling and analysis of HVDC converter by three-phase dynamic phasor,” *IEEE Trans. Power Deliv.*, vol. 29, no. 1, pp. 3–12, 2014.

[31] T. Demiray, F. Milano, and G. Andersson, “Dynamic phasor modeling of the doubly-fed induction generator under unbalanced conditions,” *2007 IEEE Lausanne POWERTECH, Proc.*, no. 2, pp. 1049–1054, 2007.

[32] S. Chandrasekar and R. Gokaraju, “Dynamic Phasor Modeling of Type 3 DFIG Wind Generators (Including SSCI Phenomenon) for Short-Circuit Calculations,” *IEEE Trans. Power Deliv.*, vol. 30, no. 2, pp. 887–897, 2015.

[33] H. W. Dommel, *Electromagnetic Transients Program Theory Book*. Vancouver, BC, Canada: Microtran Power System Analysis Corporation, 1992.

[34] E. M. G. Rodrigues, A. W. Bizuayehu, and J. P. S. Catalão, “Analysis of requirements in insular grid codes for large-scale integration of renewable generation,” in *2014 IEEE PES T&D Conference and Exposition, Chicago, IL, USA*, 2014, pp. 1–5.

[35] D. Xiang, L. Ran, P. J. Tavner, and S. Yang, “Control of a doubly fed induction generator

in a wind turbine during grid fault ride-through," *IEEE Trans. Energy Convers.*, vol. 21, no. 3, pp. 652–662, 2006.

[36] P. Kundur, *Power System Stability and Control*. McGraw-Hill, 1994.

[37] P. Kundur et al., "Definition and classification of power system stability IEEE/CIGRE joint task force on stability terms and definitions," *IEEE Trans. Power Syst.*, vol. 19, no. 3, pp. 1387–1401, 2004.

[38] J. Machowski, J. W. Bialek, and J. R. Bumby, *Power System Dynamics - Stability and Control*, 2nd ed. John Wiley & Sons, Ltd, 2008.

[39] T. Demiray, "Simulation of power system dynamics using dynamic phasor models," Ph.D. Dissertation, Swiss Federal Institute of Technology Zurich, 2008.

[40] R. H. Park, "Two-reaction theory of synchronous machines generalized method of analysis - Part I," *Trans. Am. Inst. Electr. Eng.*, vol. 48, no. 3, pp. 716–727, 1929.

[41] P. C. Krause, O. Wasynczuk, and S. D. Sudhoff, *Analysis of Electric Machinery and Drive Systems*, 2nd ed. IEEE Press, 2002.

[42] E. M. Stein and R. Shakarchi, *Fourier Analysis: An Introduction*. Princeton University Press, 2003.

[43] G. Abed, J. Lopez, M. A. Rodriguez, L. Marroyo, and G. Iwanski, *Doubly Fed Induction Machine*. IEEE Press, 2011.

[44] S. Heier, *Grid Integration of Wind Energy: Onshore and Offshore Conversion Systems*, 3rd ed., vol. 21. Wiley, 2014.

[45] "MATLAB 7 (R2016b)." The MathWorks Inc., Natick, MA, USA, 2016.

[46] N. Mohan, *Advanced Electric Drives: Analysis, Control and Modeling using MATLAB/Simulink*. John Wiley & Sons, 2014.

[47] S. Müller, M. Deicke, and R. W. De Doncker, “Doubly fed induction generator systems for wind turbines,” *IEEE Ind. Appl. Mag.*, vol. 8, no. 3, pp. 26–33, 2002.

[48] T. K. A. Brekken and N. Mohan, “Control of a doubly fed induction wind generator under unbalanced grid voltage conditions,” *IEEE Trans. Energy Convers.*, vol. 22, no. 1, pp. 129–135, 2007.

[49] P. C. Krause, F. Nozari, T. L. Skvarenina, and D. W. Olive, “The Theory of Neglecting Stator Transients,” *IEEE Trans. Power Appar. Syst.*, vol. PAS-98, no. 1, pp. 141–148, 1979.

[50] W. Gautschi, *Numerical Analysis*. Birkhäuser Boston, 2012.

[51] “Simscape Power Systems.” Hydro-Quebec and the MathWorks, Inc., Natick, MA, USA, 2016.

[52] Siemens PTI, “PSS/E Ver. 34 Online Documentation.” 2015.

[53] T. R. Byerly *et al.*, “Dynamic Models for Steam and Hydro Turbines in Power System Studies,” *IEEE Trans. Power Appar. Syst.*, vol. PAS-92, no. 6, pp. 1904–1915, 1973.

[54] IEEE Recommended Practice for Excitation System Models for Power System Stability Studies, “IEEE Std 421.5-1992,” *IEEE Std 421.5-1992*. 1992.

Appendices

Appendix A

A.1 Parameters of Wind Turbine

Symbol	Parameter	Value	Unit
c_1	Characteristic Parameters c_1	0.5176	-
c_2	Characteristic Parameters c_2	116	-
c_3	Characteristic Parameters c_3	0.4	-
c_4	Characteristic Parameters c_4	0	-
c_5	Characteristic Parameters c_5	0	-
c_6	Characteristic Parameters c_6	5	-
c_7	Characteristic Parameters c_7	21	-
c_8	Characteristic Parameters c_8	0.089	-
c_9	Characteristic Parameters c_9	0.035	-
$C_{P_{max}}$	The maximum power coefficient	0.48	-
λ_{nom}	Nominal value of tip speed ratio	8.1	-
P_m	Nominal turbine mechanical power	1.5	MW
v_{w_base}	Base wind speed	12	m/s
k_p	Power gain at $C_{P_{max}}$ and v_w are 1 p.u.	0.73	-
β	Pitch angle	0	degree

Table A.1 Parameters of Wind Turbine

A.2 Parameters of DFIG and RSC controller

Symbol	Parameter	Value	Unit
P_{nom}	Nominal Power (per one unit)	1.67	MVA
V_{nom}	Line-Line Voltage	690	V
PF	Power Factor	0.9	-
F_{nom}	Fundamental Frequency	60	Hz
R_s	Stator Resistance	0.0084	p.u.
L_{ls}	Stator Leakage Inductance	0.167	p.u.
R_r	Rotor Resistance	0.0083	p.u.
L_{lr}	Rotor Leakage Inductance	0.1323	p.u.
L_m	Mutual Inductance	5.419	p.u.
H	Inertia Constant	5.5	s
p	Number of Pole Pairs	2	-
K_{I1}	integral controller gain – *d*-axis	0.7301	-
K_{I2}	integral controller gain – *q*-axis	0.7301	-
K_{P1}	proportional controller gain – *d*-axis	0.0149	-
K_{P2}	proportional controller gain – *q*-axis	0.0149	-

Table A.2 Parameters of DFIG

A.3 Parameters of Two-area Four-machine test case

Symbol	Parameter	Value	Unit
1) Generators			
V_n	Line-to-line voltage	20,000	Vrms
f	Frequency	60	Hz
X_d	*d*-axis synchronous reactance	1.8	p.u.
X_q	*q*-axis synchronous reactance	1.7	p.u.
X_l	Leakage reactance	0.2	p.u.
X'_d	*d*-axis transient reactance	0.3	p.u.
X'_q	*q*-axis transient reactance	0.55	p.u.
X''_d	*d*-axis subtransient reactance	0.25	p.u.
X''_q	*q*-axis subtransient reactance	0.25	p.u.
R_s	Stator winding resistance	0.0025	p.u.
F	Friction factor	0	p.u.
p	Pole pairs	4	-
T'_{d0}	*d*-axis transient open-circuit time constant	8.0	s
T'_{q0}	*q*-axis transient open-circuit time constant	0.4	s
T''_{d0}	*d*-axis subtransient open-circuit time constant	0.03	s
T''_{q0}	*q*-axis subtransient open-circuit time constant	0.05	s
H_1	Inertia coefficient for generator G1 and G2	6.5	s
H_2	Inertia coefficient for generator G3 and G4	6.175	s
2) Transmission lines (230 kV, 100 MVA Base)			
r	0.0001	0.0001	p.u./km
x_L	0.001	0.001	p.u./km
b_C	0.00175	0.00175	p.u./km
3) Step-up transformer (20/230 kV, 900 MVA Base)			
r	0	0.0001	p.u.
x_t	0.15	0.001	p.u.

Table A.3 Parameters of two-area four-machine network.

Appendix B

B.1 State Space Model of Synchronous Machine

In Chapter 5, the following synchronous generator model is used for test case including stator dynamics in the rotor reference frame (*DQ* reference frame) as

$$V_d = R_s i_d + \frac{d}{dt}\varphi_d - \omega_R \varphi_q, \qquad \varphi_d = L_d i_d + L_{md}(i'_{fd} + i'_{kd}) \tag{B.1}$$

$$V_q = R_s i_q + \frac{d}{dt}\varphi_q + \omega_R \varphi_d, \qquad \varphi_q = L_q i_q + L_{mq} i'_{kq} \tag{B.2}$$

$$V'_{fd} = R'_{fd} i'_{fd} + \frac{d}{dt}\varphi'_{fd}, \qquad \varphi'_{fd} = L'_{fd} i'_{fd} + L_{md}(i_d + i'_{kd}) \tag{B.3}$$

$$V'_{kd} = R'_{kd} i'_{kd} + \frac{d}{dt}\varphi'_{kd}, \qquad \varphi'_{kd} = L'_{kd} i'_{kd} + L_{md}(i_d + i'_{fd}) \tag{B.4}$$

$$V'_{kq1} = R'_{kq1} i'_{kq1} + \frac{d}{dt}\varphi'_{kq1}, \qquad \varphi'_{kq1} = L'_{kq1} i'_{kq1} + L_{mq} i_q \tag{B.5}$$

$$V'_{kq2} = R'_{kq2} i'_{kq2} + \frac{d}{dt}\varphi'_{kq2}, \qquad \varphi'_{kq2} = L'_{kq2} i'_{kq2} + L_{mq} i_q \tag{B.6}$$